

**HIGH RESOLUTION ZERO DEGREE AUGER ELECTRON SPECTROSCOPY
OF DOUBLY EXCITED HELIUM-LIKE RESONANCE STATES OF BORON,
MAGNESIUM AND SILICON**

by

HABIBOLLAH ALIABADI

B.S., Marshall University, 1990

M.S., Miami University, 1993

A DISSERTATION

submitted in partial fulfillment of the

requirements for the degree

DOCTOR OF PHILOSOPHY

**Department of Physics
College of Arts and Sciences**

**KANSAS STATE UNIVERSITY
Manhattan, Kansas**

2004

Approved by:

Major Professor

Patrick Richard

**HIGH RESOLUTION ZERO DEGREE AUGER ELECTRON SPECTROSCOPY
OF DOUBLY EXCITED HELIUM-LIKE RESONANCE STATES OF BORON,
MAGNESIUM AND SILICON**

by

HABIBOLLAH ALIABADI

B.S., Marshall University, 1990

M.S., Miami University, 1993

AN ABSTRACT OF A DISSERTATION

submitted in partial fulfillment of the

requirements for the degree

DOCTOR OF PHILOSOPHY

**Department of Physics
College of Arts and Sciences**

**KANSAS STATE UNIVERSITY
Manhattan, Kansas**

2004

ABSTRACT

High-resolution zero-degree Auger-electron spectroscopy was conducted on hydrogen-like fluorine, boron, magnesium and silicon ions colliding with a thin molecular hydrogen gas target. Absolute doubly-differential ion-atom collision cross sections were measured by collecting target electrons scattered from projectile ions. The electrons were scattered directly (non-resonantly) or resonantly through auto-ionizing doubly-excited helium-like states of the projectile ions. Differential resonant and non-resonant collision cross sections for quasi-free electron-ion collisions were then extracted from the ion-atom collisions cross sections by deconvoluting the momentum profile of the bound target electrons. The measured cross sections for direct and resonant elastic scattering collisions for fluorine were in good agreement with previous experimental results and theoretical predictions. An enhancement was observed in the BEe peak in the collisions of $42\text{MeV } Mg^{11+} + (30mT) H_2$. A resonance peak associated with the elastic scattering from the $2p^2\ ^1D$ doubly-excited state of the ion was observed. The measured cross section and the calculated R-matrix electron-ion cross section for this collision system agree very well. Only direct scattering cross sections were measurable in collisions of hydrogen-like Si due to limited ion beam intensity. No measurable enhancement in the cross section of the binary encounter electron (BEe) peak of $70\text{MeV } Si^{12+,13+} + (30mT) H_2$ was observed in comparison with the calculated BEe peak for the bare silicon ions. Similar experiments were planned for the inelastic resonant scattering of electrons from the $3\ell n\ell'$, ($n = 3, 4, \dots$ series limit) doubly-excited states of these

ions in order to measure the electron impact $1s \rightarrow 2\ell$ excitation cross section. The lack of ion beam intensity prohibited the study of this excitation process for these ions. However, the excitations of the $3\ell 3\ell'$ resonance states were studied in the collisions of $5.38\text{MeV } B^{4+} + (20\text{mT}) H_2$. Multiple resonance peaks corresponding to $3lnl' \rightarrow 2l$ ($n=3-10$) were observed. The electron impact excitation cross sections calculated in the R-matrix method agrees very well with the measured cross sections for $3\ell 3\ell'$ manifold in this process. The cross sections obtained in this study are among the few electron differential scattering cross sections available in the literature due to the difficulties involved in conducting electron-ion collision experiments. The present experiments serve as rigorous tests of the current theoretical methods of calculating electron-ion scattering cross sections. The short range electron-ion interactions are predicted to be strongest in 180° scattering in the center of mass frame. 180° scattering in the center of mass is observed at zero degrees in the laboratory frame which is the angle of observation of electrons in this dissertation.

TABLE OF CONTENTS

<i>LIST OF FIGURES</i>	<i>ii</i>
<i>LIST OF TABLES</i>	<i>v</i>
ACKNOWLEDGEMENTS.....	<i>vi</i>
<i>Chapter One</i>	<i>1</i>
Introduction.....	<i>1</i>
<i>Chapter two</i>	<i>8</i>
High Voltage Double Parallel Plate Electron Spectrometer	<i>8</i>
<i>Chapter Three</i>	<i>25</i>
Zero Degree Electron Spectroscopy	<i>25</i>
Collision kinematics.....	<i>25</i>
Experimental setup.....	<i>27</i>
<i>Chapter Four</i>	<i>36</i>
Preliminary test experiments.....	<i>36</i>
Calculation of cross sections from experimental results.....	<i>38</i>
<i>Chapter Five</i>	<i>53</i>
Experiments with boron, fluorine, magnesium and silicon	<i>53</i>
Impulse approximation method and the electron scattering model	<i>54</i>
Determination of RTEA scattering cross sections	<i>59</i>
<i>Conclusions</i>	<i>86</i>
<i>References</i>	<i>89</i>

LIST OF FIGURES

Figure 1 Electron energy spectrum for the collision of 19 MeV $F^{9+} + H_2$ observed at 0° showing the cusp and binary encounter peaks.. 6

Figure 2 Side-view of the collision chamber is seen in this picture. Alignment tables can be seen in this picture. 11

Figure 3 Top view of the collision chamber is depicted here. 13

Figure 4 The DPC, the spectrometer assembly and the channeltron detector inside the collision chamber are illustrated. The spectrometer shielding is removed for the photograph. 15

Figure 5 Hydrogen gas pressure inside the DPC, collision chamber and the beamline as a function of pressure inside the gas cell is graphed. 17

Figure 6 Pressure dependence for the yield of the $2p^2 \ ^1D$ resonance line observed in 22 MeV F^{8+} colliding with hydrogen molecules is depicted..... 18

Figure 7 A schematic of the zero degree tandem electron spectrometer is shown.. . 20

Figure 8 The top panel shows an electron beam profile resolved by the spectrometer. 23

Figure 9 A parallel plate spectrometer and some of its parameters are depicted. .. 24

Figure 10 The velocity of the scattered electron in the laboratory frame of reference, v , is determined by the addition of the electron velocity in the projectile frame, v' , to the velocity of the projectile V 26

Figure 11 A schematic of the experimental setup: the ions are accelerated in the Van de Graaff accelerator and the LINAC to the required energy.. 30

Figure 12 A schematic of applied voltages to the double parallel plate spectrometer is depicted..	32
Figure 13 A schematic of the electronics set up for the experiments..	34
Figure 14 5.5 MeV boron ions were collided with Ne gas to investigate the possibility of the production of Fermi shuttle electrons.....	41
Figure 15 Low resolution electron spectrum of hydrogen-like silicon colliding with a target gas taken at zero degree angle of scattering.....	43
Figure 16 Electron spectra of hydrogen-like fluorine colliding with a hydrogen target gas are depicted.....	44
Figure 17 Electron spectrometer transmission is depicted. As expected the transmission curves overlap and exhibit a $\frac{1}{F}$ behavior. The green line is a $\frac{1}{F}$ fit to the fluorine data.....	45
Figure 18 The calculated binary encounter electron cross sections for different ions are demonstrated..	49
Figure 19 The BEe peak is matched to the Auger energy of the electrons decaying from the doubly excited state of the ion to the ground state in order to create the doubly excited states.....	51
Figure 20 Kinematics of a target electron in the projectile rest frame is depicted...	56
Figure 21 Measured doubly differential cross section for the collisions of the hydrogen-like magnesium ions with a thin molecular hydrogen target gas is depicted..	66
Figure 22 The differential cross sections of collisions of electrons with the hydrogen-like magnesium ions for the $2\ell 2\ell'$ manifold is depicted.....	68

Figure 23 Experimental differential cross sections for the collisions of electrons with hydrogen-like magnesium ions is determined through collisions of hydrogen-like magnesium ions with a thin molecular hydrogen target gas.. 70

Figure 25 Resonant excitation strength for the $(2p^2)^1D$ line for various hydrogen-like ions..... 72

Figure 24 The measured cross sections of the BEE peaks for $\text{Si}^{12+,13+}$ presented in this picture.. 73

Figure 26 The full zero degree electron spectrum of collisions of hydrogen-like boron with a molecular hydrogen target can be seen here.. 78

Figure 27 The differential cross sections for collisions of hydrogen-like boron with molecular hydrogen is depicted.. 80

Figure 28 The theoretically calculated cross sections for the collisions of electrons with hydrogen-like boron ions differential in the solid angle is depicted.. 82

Figure 29 The measured cross sections as well as the theoretical calculation is shown in an expanded view. The terms of the $3\ell 3\ell'$ manifold are identified in this picture. 84

LIST OF TABLES

Table 1 Diameter of the circular titanium apertures used in the gas cell.....	10
Table 2 Design parameters for the two stages of the spectrometer. The spectrometer constants and the energy resolutions are pure numbers. The rest of the values are in inches.	24
Table 3 Length of resonators and the maximum amount of boost they can provide.	28
Table 4 Detection efficiency for various electron pass energies is tabulated.....	40
Table 5 Compton profile parameters for the hydrogen molecule and the helium atom.....	58
Table 6 The $(2p^2)^1D$ line resonance parameters for various ions is presented. Z is the atomic number and E_A is the resonance Auger energy. A_r and A_a are the radiative and Auger decay rate and ξ is the Auger yield. a) from ref [98], b) from ref [97], c) from ref [99] and d) from ref [31].	75
Table 7 The ratio of DDCS for non bare to bare ions, R , is known as the enhancement factor. This factor was determined for various ions from equation 4.1 having determined the detection efficiency of the spectrometer in advance (see Table 4). The relative error for the calculation of R is ~15%.	75

ACKNOWLEDGEMENTS

I would like to acknowledge the people who have supported me in this endeavor. I would like to thank my advisor Professor Patrick Richard for his support. He has been a model for me to emulate professionally as well as personally. Pat supported me during some very personally trying times that I went through. I would also like to thank the members of my advisory committee. Especially I would like thank Professor Thomas W. Gorczyca for doing all the needed R-matrix calculations and I would like to thank Professor C. Lewis Cocke for the several conversations I had with him regarding my research. The Faculty and staff of the J R Macdonald Laboratory made this dissertation possible with their support. Professor Carnes and Mr. Vincent Needham were always happy to provide assistance in the operations of the Tandem Van de Graaff accelerator as well as the LINAC accelerator. Their expert help in the operations of the Data acquisition systems was also indispensable. Mr. Robert Krause provided the needed ion beams for the experiments and made the operation of the Tandem accelerator go smoothly. Mr. Mike Wells and Mr. Al Rankin built the beamline that I needed for this experiment and they aligned the collision chamber. They also assisted me with the operations of the vacuum systems and from time to time they also assisted in solving the problems of beam tuning. Visiting professor Mark Gealy designed the alignment tables and the differentially pumped chamber and gas cell. Mr. Bob Geering built the components of the system that we designed. Finally Mr. Scott Chainey provided support for the electronics that I needed for my experiments. I am very grateful to all of them. I would also like to thank the department of Physics and its faculty and staff as well as the Kansas State University as a

whole. Special thanks go to Dea Richard. She proofread and made many suggestions to improve my manuscripts and gave me moral support.

I would also like to thank my family for their moral support, especially our parents, my wife and my sisters.

This work was financially supported by the Chemical Sciences, Geosciences and the Biosciences Division, Office of Basic Energy Sciences, Office of Science, the U.S. Department of Energy.

Chapter One

Introduction

Electron-ion collision cross sections have been of interest in the past decades [1-14]. These cross sections provide insight into the mechanisms involved in diverse fields such as astrophysics, thermonuclear physics and the physics of lasers. In recent years our ability to measure such cross sections differentially in energy and angle has enhanced the understanding of how particles in a plasma, a reactor or a heavenly body exchange energy or cool due to radiation or scattering. Theoretical calculations have also become evermore sophisticated. Theoretical calculations are capable of approximating differential cross sections for such collisions, and they can be done with powerful computers rather rapidly [14]. The validity of various approximations which influence the calculated differential cross sections in such calculations can be tested by comparing their results with the results of experimental measurements.

Recently more attention has been given to large angle electron ion scattering cross sections. Theoretical calculations suggest that in large angle scatterings the more sensitive short range interactions between the electrons and ions may be probed with more accuracy [14-18]. Collisions of electrons with multiply charged ions are of special interest since the correlated interaction of the impinging electrons and the electrons on the projectile may be more readily studied. During such collisions the electrons may

scatter off the projectile ions directly or resonantly, and the electrons may retain, gain or lose some of their energy during the interaction. Correspondingly such collisions may be categorized as elastic, superelastic or inelastic [19, 20]. A resonance collision occurs when the impinging electrons with a correct specific energy collide with the ion. This process is known as a radiationless capture (RC) [21]. An RC is stabilized either by the emission of an Auger electron [22, 23] or a photon. Dielectronic recombination [24-26], DR, is the final outcome of RC if the ion-charge is stabilized by photon decay.

In the case of an electron-ion interaction the resonance is marked by the capture of the incoming electron and the simultaneous excitation of an electron on the target ion. In this sense the RC is a hallmark of the electron-electron interaction in such collisions. If after a non resonant (direct) or resonant collision, the ion is left with more energy than before the collision the process is known as an electron impact excitation or inelastic scattering. The scattered electrons carry off less energy and indicate the degree of inelasticity of the scattering process.

Ion- atom experiments have also been a subject of interest for similar reasons [27-29]. In such experiments the ions are accelerated through a potential difference and then directed to collide with the atoms in a thin target gas. After the collisions some of the fragments and/or the photons leaving the collision area are collected in order to study the collision mechanisms. In this scheme the projectile ions are separated from the electrons by some active element such as a magnet or an electrostatic device. One of such experimental techniques is the zero-degree electron spectroscopy [30-32]. In this type of

experiment after the collision the ions are collected at a Faraday cup and the zero degree scattered electrons are energy analyzed through an electron spectrometer and detected. A typical zero-degree spectrum of electrons can be seen in Figure 1. Such spectra show a large yield of low-energy electrons followed by cusp electrons which travel at the same speed as the projectile ion and the binary encounter electrons (BEe) which travel at about twice the speed of the projectile ion. The low-energy ions are the result of distant (or soft) collisions between the projectiles and the target [34, 35]. The cusp electrons are the result of capture of the target electrons to the continuum of the projectile (ECC) or loss of projectile electrons to its continuum (ELC) [29]. The BEe results from head-on collisions between the projectiles and the target electrons [33]. The width of the BEe peak is a reflection of the Compton profile of the target electrons. In addition to these general features in the zero-degree electron spectrum, resonance peaks may also be observed if the electron energy spectrum is taken in a sufficiently high resolution. Such resonance peaks are due to the capture of the target electrons to an intermediate state of the ion and the subsequent Auger decay of that state. The Auger-electron decay channels are in competition with the possible photon-decay channels.

It is possible to make autoionizing states of the projectiles by multiple electron captures or by ionization of an equal or greater than three electron projectile ions. The latter such electrons are not a part of this study.

The resonant capture of an electron from the target to an excited state of the ion and the simultaneous excitation of the ion's electron is known as resonant transfer and

excitation (RTE) [36-38]. RTE is a correlated electron-electron process and can be seen to be the reverse of the Auger decay of the same state of the ion. A non resonant capture and excitation is known as NTE [38-42]. In this case a target electron is captured by the projectile and one of the ion's electrons is promoted to the excited state by the nucleus of the target. NTE is a significant process if the target nucleus is heavy. For light targets NTE does not play a significant role except at low bombarding energies.

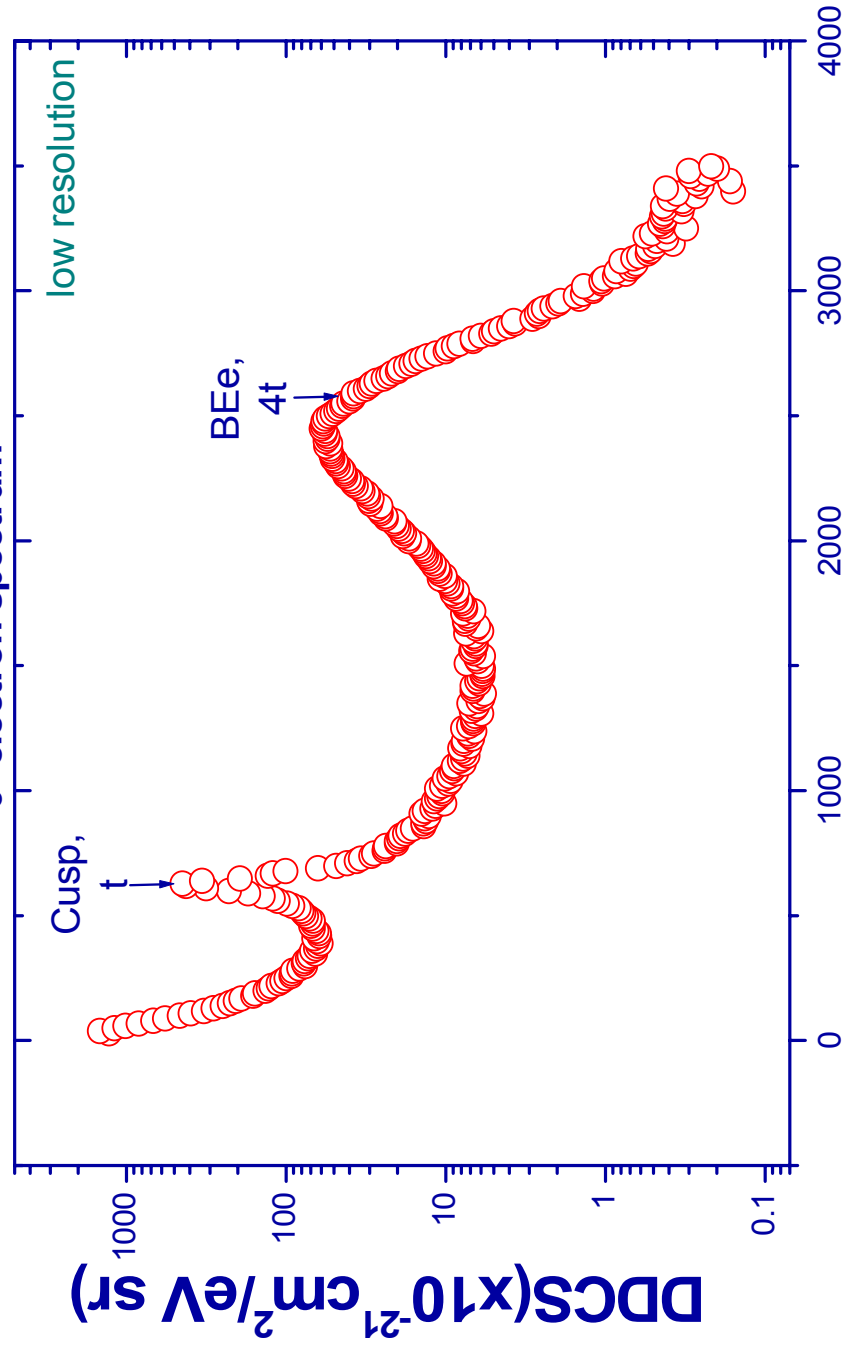
In cases where the target electron may be considered to be the only participant in the collision, one may speak of the "quasi-free" electrons of the target colliding with the projectile ion. The quasi-free electrons possess a momentum distribution, known as the Compton profile, due to being bound to the target nucleus. As a consequence the projectiles which are impinged upon by the quasi-free electrons are exposed to a distribution of electron energies. The similarity of the collisions of quasi-free electrons with ions and the collisions of free electrons with ions became the inspiration to develop the Electron Scattering Model (ESM) [33, 43-45]. In this model the cross sections of collisions of quasi-free electrons impinging on ions are taken as the calculated cross sections of collisions of mono-energetic free electrons with the same ion. The ESM in conjunction with ion-atom scattering is now used as a novel technique to determine electron-ion scattering cross sections. Such experiments with traditional merged beam or crossed beam configuration are especially hard to perform for large angle scatterings and for many discrete electron energies due to low electron beam luminosity and other experimental difficulties. No differential electron scattering data for electron-ion collisions have been performed at sufficient electron energies to observe resonances.

Resonances have only been observed in the DR channel in electron-ion collisions in the storage rings [46, 47]. Since large angle electron-ion scattering is most interesting in the study of electron-electron interactions, the ESM and zero-degree Auger-electron spectroscopy is used to study direct and resonance interactions in this dissertation.

Figure 1 Electron energy spectrum for the collision of 22 MeV F^{8+} + 30 mT H_2 observed at 0° in low resolution. The figure shows the cusp and the binary encounter electron peaks. The cusp is at energy t and the binary encounter electron peak is located at energy slightly lower than $4t$.

$22\text{MeV F}^{8+} + 30\text{ mT H}_2$

0° electron spectrum



Chapter two

High Voltage Double Parallel Plate Electron Spectrometer

A high resolution double 45° parallel-plate electron spectrometer, gas cell and chamber system was designed, constructed and placed in operation in the JRML in 1986. This system is described in quite detail in the Ph.D. dissertation of D. H. Lee [48]. The system was only capable of sustaining 3kV and suffered from moderate vacuum conditions. To have an electron spectrometer of comparable energy resolution and detection efficiency but capable of sustaining much higher voltage and therefore analyzing much higher energy electrons was desirable. It was also desirable to construct the system on an optical bench for ease of ion beam and spectrometer alignment.

To meet the new design features a new gas cell and a parallel plate spectrometer were designed. The new system can be aligned to better than 0.1 inch. The gas cell is 12 cm long and it is doubly differentially pumped. The spectrometer assembly is capable of maintaining high voltages in order to analyze energetic electrons. Better alignment and isolation of the spectrometer from the rest of the collision system reduces the possibility of rescattered electrons entering the spectrometer. The gas cell and the spectrometer assemblies are mounted on individual tables (see Figures 2 through 4). These tables may be moved perpendicularly or horizontally so that the gas cell and spectrometer assemblies will allow the passage of the incoming beam of ions without significant scattering within

the spectrometer system. The collision region is made up of a 12 centimeter long gas cell enclosed within a differentially pumped chamber (DPC). The gas cell is electrically isolated from the ground so that it may be floated. The circular titanium apertures on the cell and the DPC are also isolated from the ground with ceramic washers. These apertures may be floated to several hundred volts. The tightest aperture is the entrance to the gas cell (see Table 1). Further downstream the apertures are somewhat larger in size. This configuration of sizes in the apertures was chosen to reduce the number of electrons created up-stream outside the collision region from making their way into the cell and ultimately into the spectrometer. To maintain the vacuum inside the spectrometer the DPC and the Faraday cup are pumped by two 210 liters/s turbo pumps and the entire collision chamber is pumped by a 520 liters/s turbo pump. The Gas pressure in the collision chamber and the beamline can be maintained to two orders of magnitude lower than the pressure inside the gas cell (Figure 5). This condition is true for pressures nearing 30 millitorr. The condition for single collisions has been tested for the case of 22 MeV F^{8+} projectiles incident on molecular hydrogen gas as a target (Figure 6) [32, 49-51]. A linear relationship between the collected electron and the gas pressure indicates what is known as a single collision condition. At higher pressures the relationship is exponential indicating electron capture or loss by the projectile. For most experiments performed the pressure was kept at 30 millitorr to assure a single collision condition. In the case of the lower energy projectiles used in this work the pressure was kept at 20 millitorr.

Gas cell aperture	Gas cell aperture size in millimeters
1	2.5
2	3
3	4
4	4

Table1 Diameter of the circular titanium apertures used in the gas cell.

Figure 2 Side-view of the collision chamber is seen in this picture. Alignment tables can be seen in this picture.

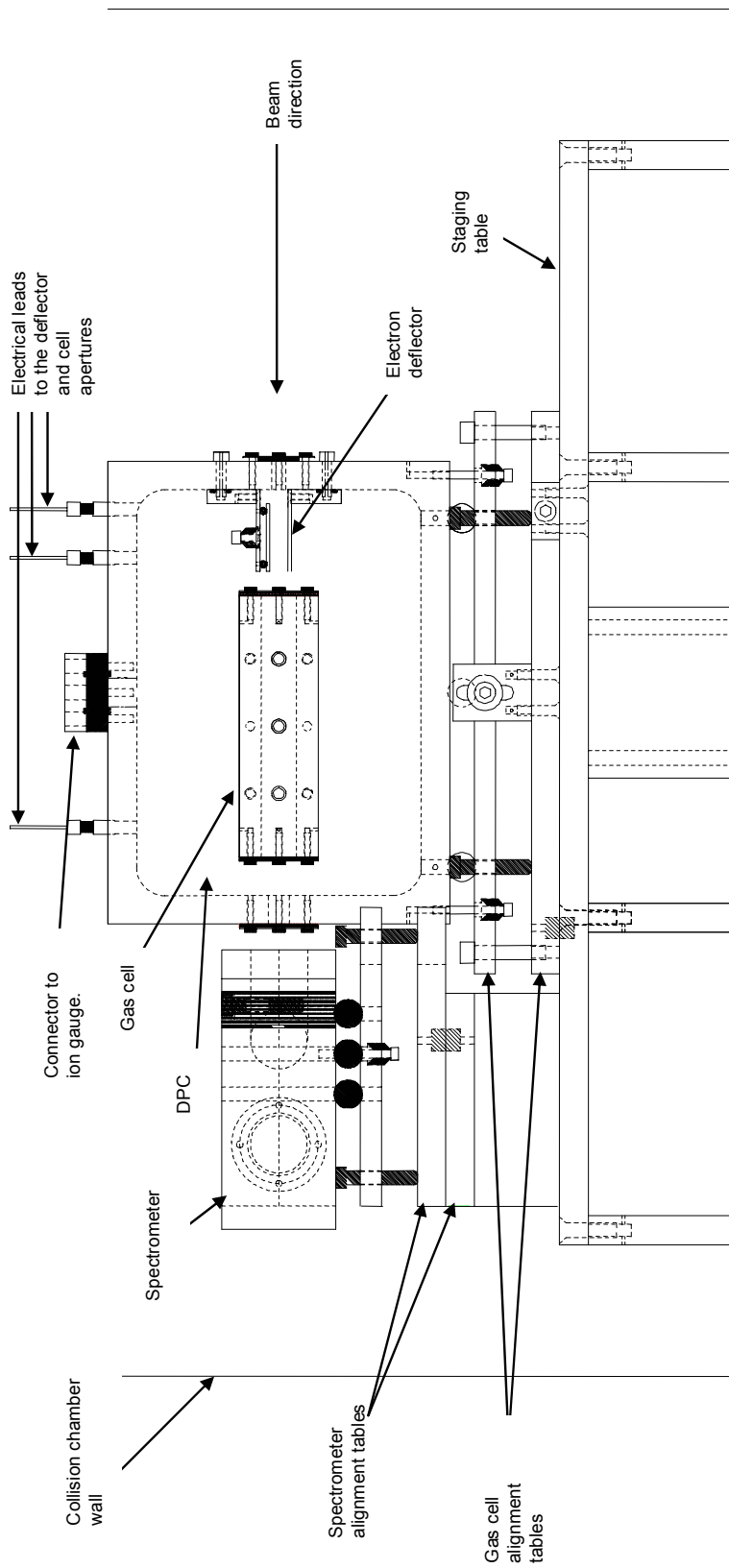


Figure 3 Top view of the collision chamber is depicted here.

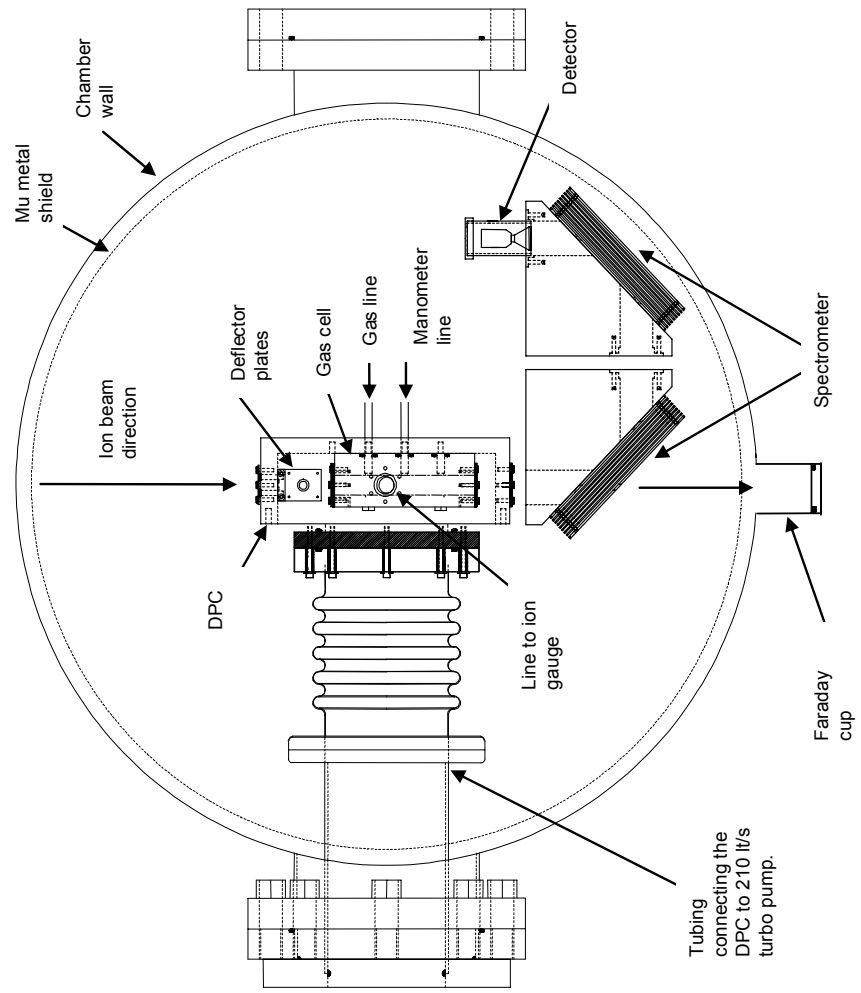
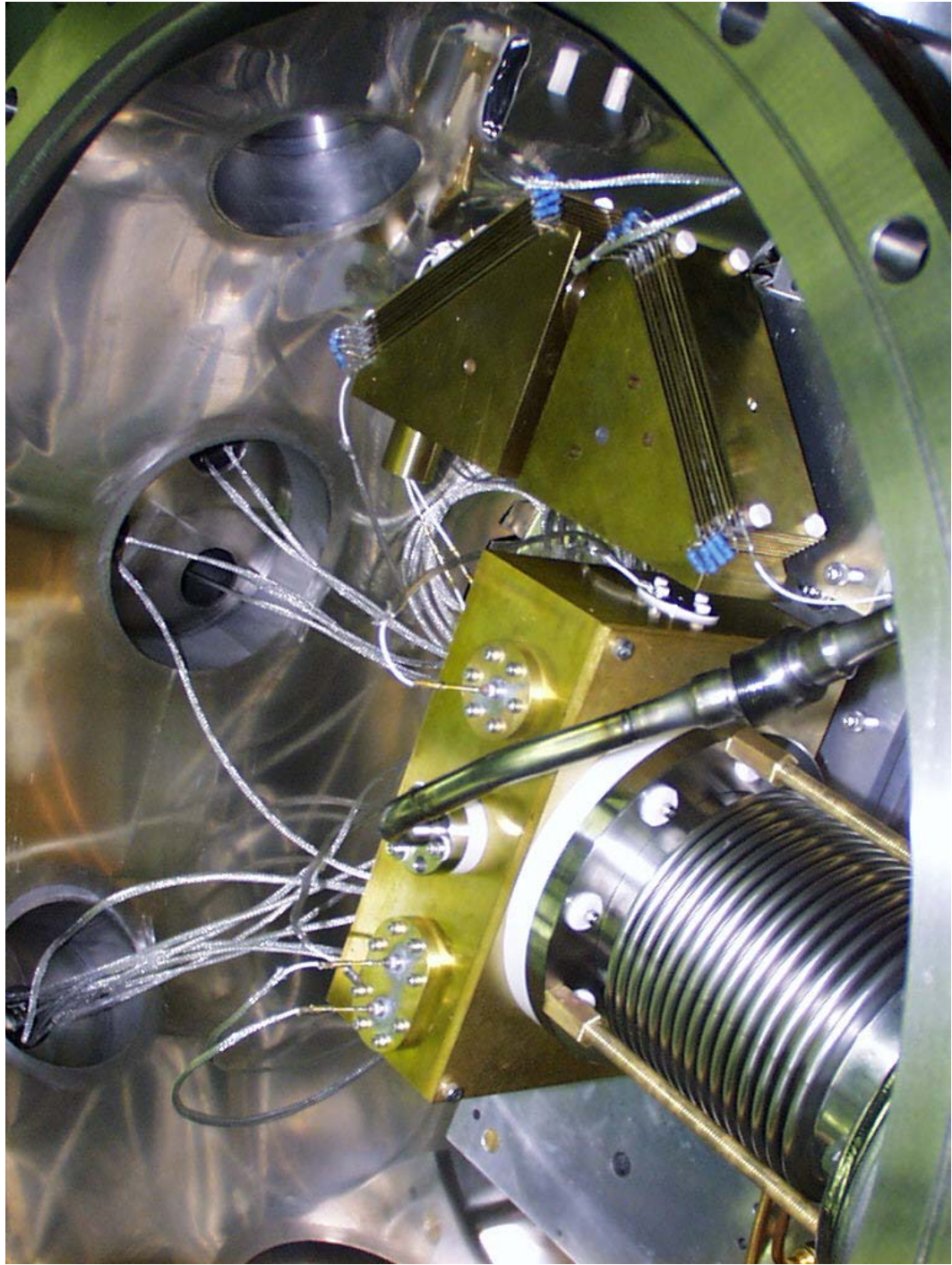


Figure4 The DPC, the spectrometer assembly and the channeltron detector inside the collision chamber are illustrated. The spectrometer shielding is removed for the photograph.



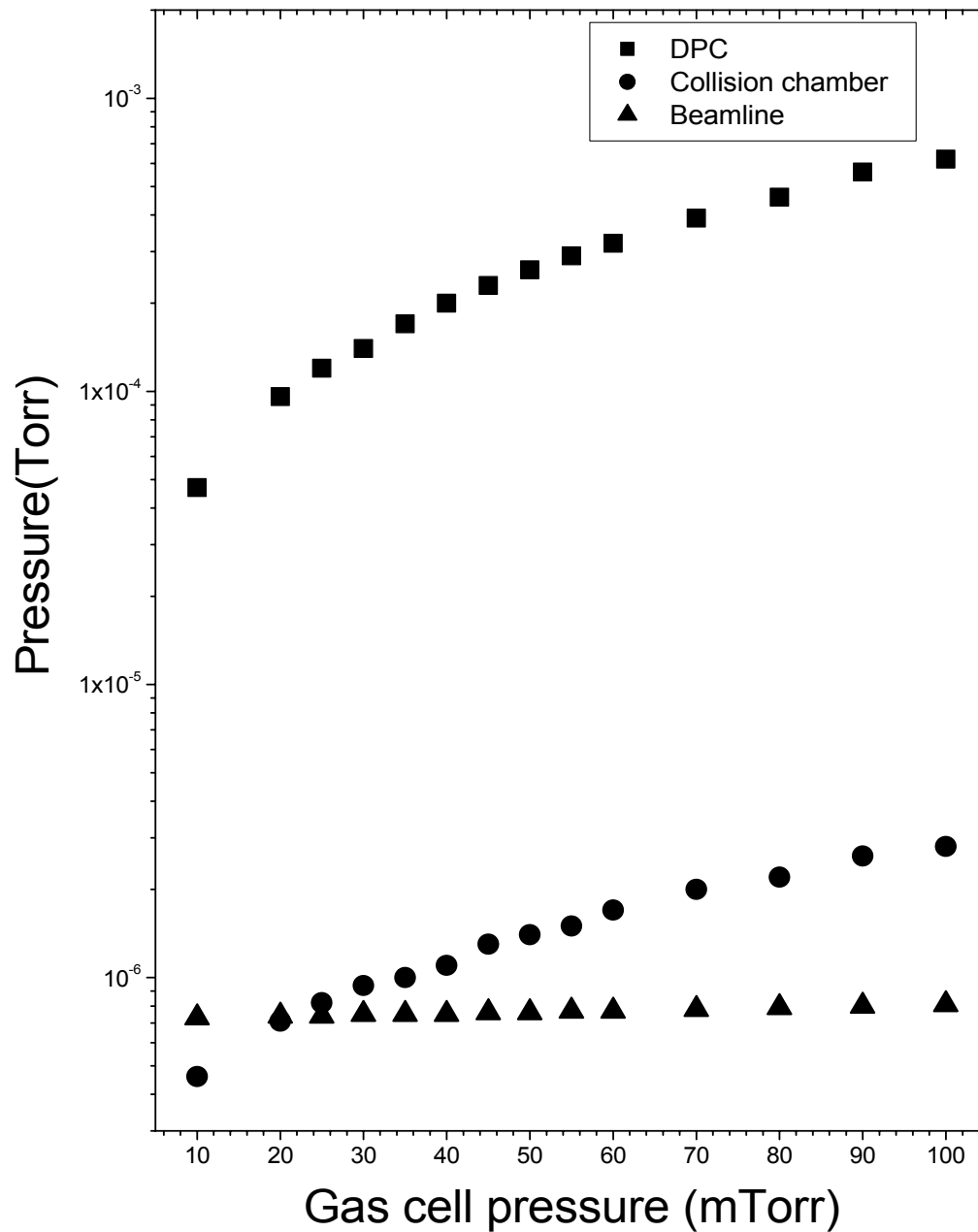


Figure 5 Hydrogen gas pressure inside the DPC, collision chamber and the beamline as a function of pressure inside the gas cell is graphed.

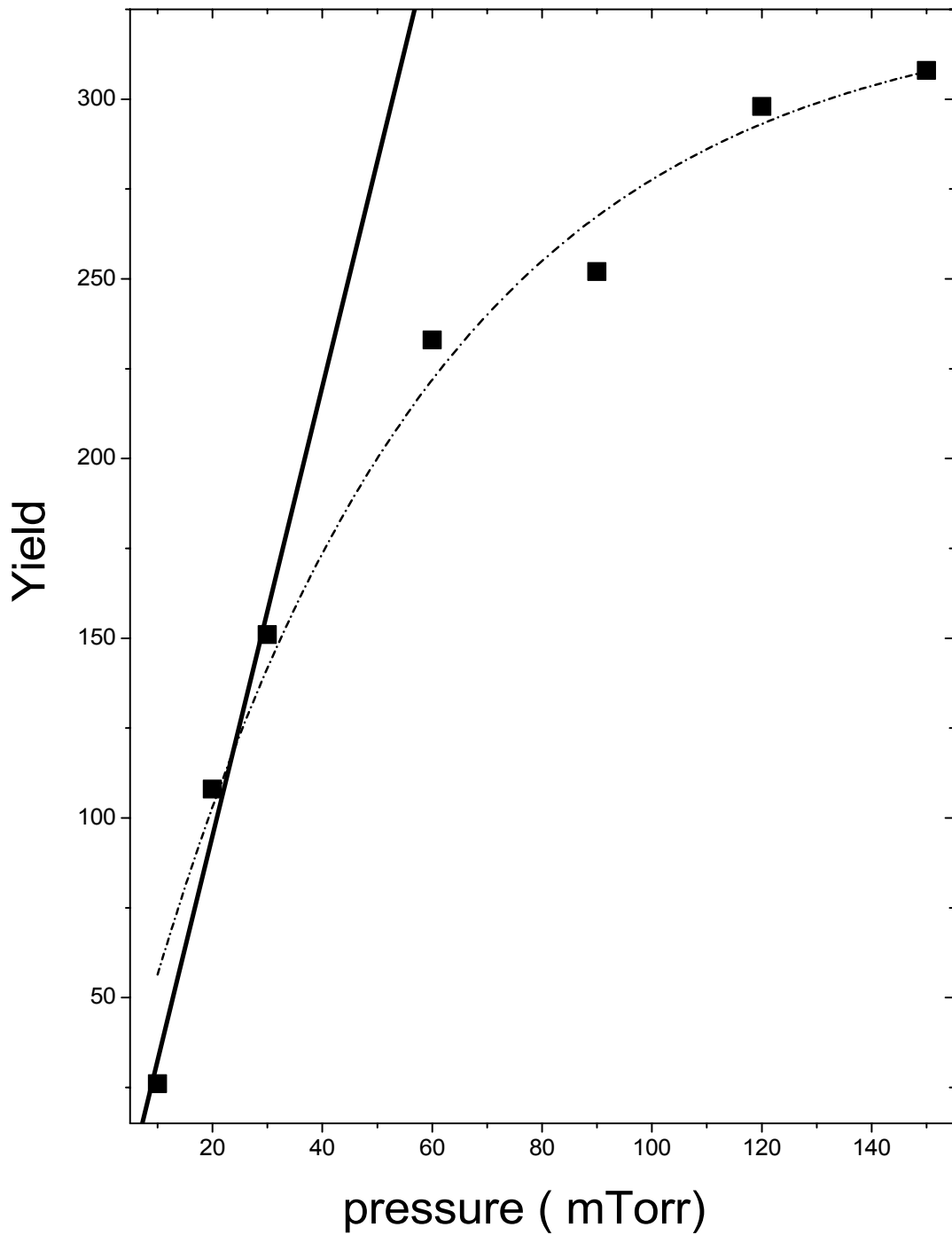


Figure 6 Pressure dependence for the yield of the $2p^2\ ^1D$ resonance line observed in 22 MeV F^{8+} colliding with hydrogen molecules is depicted. The solid line is the linear fit to the first three points. The dash dotted line is an exponential fit to the data. The exponential fit indicates the adverse effect of multiple collisions on the number of electrons collected.

The gas cell and spectrometer were built from brass. Brass was chosen since this metal is easier to clean and appears to oxidize at a slower rate than aluminum. Oxidation of the surfaces and collection of hydrocarbons from the mechanical pumps have been identified as possible sources of unwanted background electrons in the spectrometer [52]. These extraneous electrons distort the collected spectra.

The double parallel plate electron spectrometer is a well known design used for the purpose of zero degree electron spectroscopy [51]. Figure 7 depicts this spectrometer in more detail. The plates of this spectrometer are separated with ceramic beads. These beads withstand high voltages [53]. The plates of the spectrometer are 1.6 mm apart. Each stage of the spectrometer is comprised of nine plates. The first and the last plate constitute a condenser. The seven plates in between are hollow in the middle and their presence creates a more uniform electric field. The plates of the spectrometer are connected in series through 1 M Ω resistors. Each stage of the spectrometer is at a 45 degree angle relative to the incoming beam of the electrons. The back plate of the first stage is fitted with a 4.5 millimeter aperture for the purpose of letting the incident ion beam out of the spectrometer and into the Faraday cup. The two stages are placed such that the exit surface of the first and the entrance surface of the second are in parallel and they are placed at 1 centimeter from each other. A potential difference may be applied between the two stages for a high resolution scan of the scattered electrons. At the exit of the second stage the electrons are detected by a channel electron multiplier. The flight path of the electrons from the center of the gas cell to the channeltron is 30 cm long.

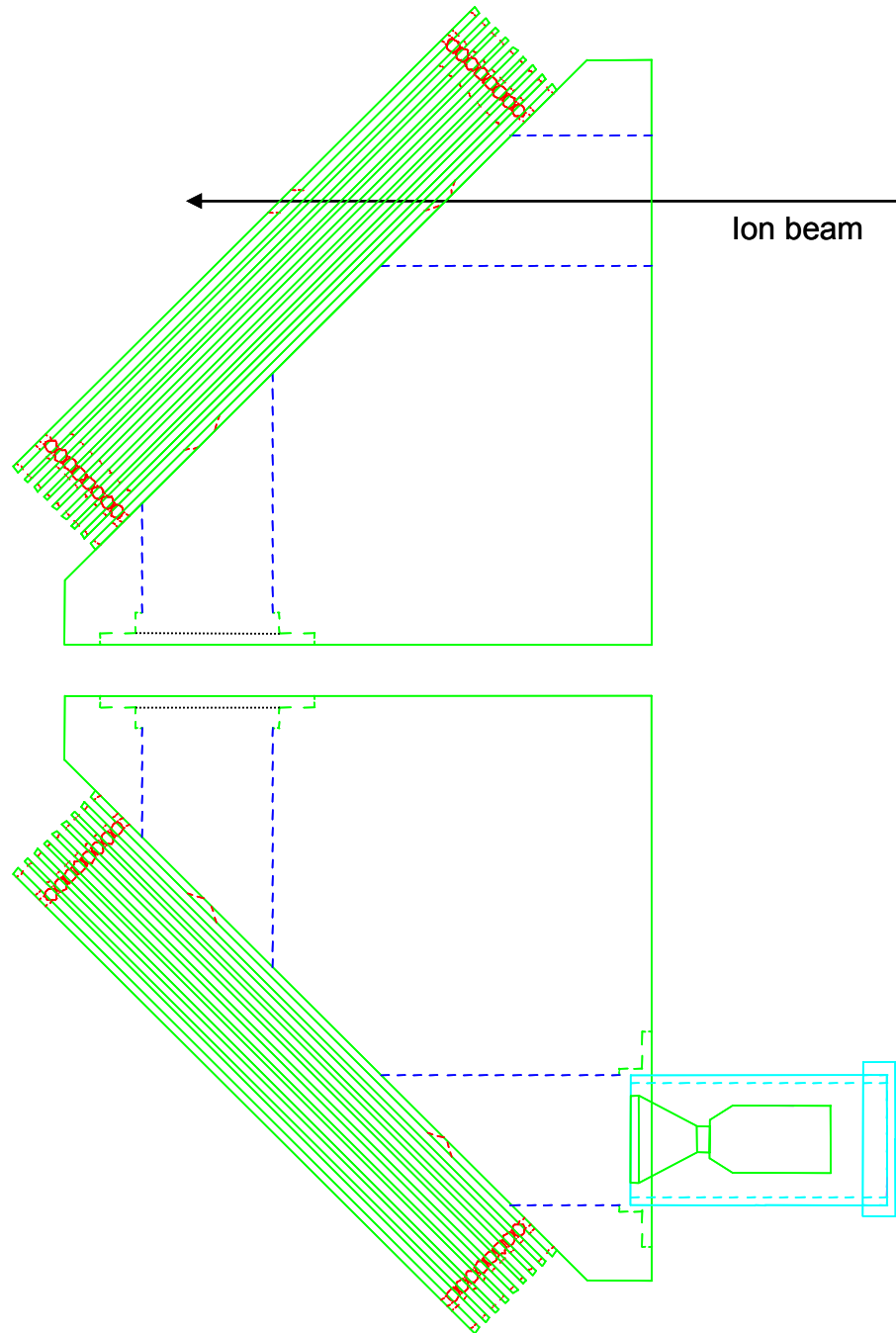


Figure 7 A schematic of the zero degree tandem electron spectrometer is shown. The slits are indicated with broken slanted lines intersecting the solid lines delineating the plates. The incoming beam and the zero degree scattered electrons make a 45° angle to the analyzer plates. A channel electron multiplier is placed at the exit of the second stage.

The spectrometer was at first tested with an electron gun to determine the spectrometer constants of the two stages of the spectrometer. The electron gun was placed near the entrance of the spectrometer. The spectrometer constant for the first stage was determined by placing a channeltron at the exit of that stage and varying the voltage so that a peak transmission of electrons was detected by the detector. The same technique was employed for the second stage. Since in the high resolution mode the second stage is capable of analyzing electron energies in less than 1 eV increments, the second stage spectrometer constant is determined more precisely by placing the two stages in tandem in a high resolution mode and scanning for the best transmission of the electrons through the second stage.

Figure 8 shows the Gaussian profile of an electron beam observed in high resolution. Each stage of the spectrometer has physical characteristics that determine its resolution and analyzer constant (see Table 2). The resolution of each stage is determined by the width of the slits on the first plate (w_1 and w_2) of the stage and the separation of the slits (L) [50]:

$$R = \frac{\Delta E}{E} = \frac{(w_1 + w_2)}{2L} \quad (2.1)$$

This formula is valid for the electrons entering the stage at a 45 degree angle. The spectrometer constant for each stage depends on the separation of the field plates (d) of

that stage (the first and the last plates) and the distance of separation of the slits on the first plate:

$$f = \frac{2d}{L} = \frac{eV}{E} \quad (2.2)$$

Figure 9 shows how these parameters are related to a parallel plate spectrometer. E is the energy of the analyzed electrons; V is the voltage applied to the plates; and e is the electron charge. This formula also assumes the trajectory of the incoming electrons is at a 45 degree angle relative to the plates of the spectrometer.

Spectra may be analyzed in high resolution by decelerating the electrons between the two stages. Since the resolution of the second stage depends on geometrical factors only, the decelerated electrons now moving through the second stage at a much lower energy, known as the pass energy, can be detected with a much smaller variance in the energy. The ratio of the electrons' original incident energy, E , to the pass energy, E_{pass} , is known as the deceleration factor, F . The higher the deceleration factor the smaller is the energy variance in the observed spectrum.

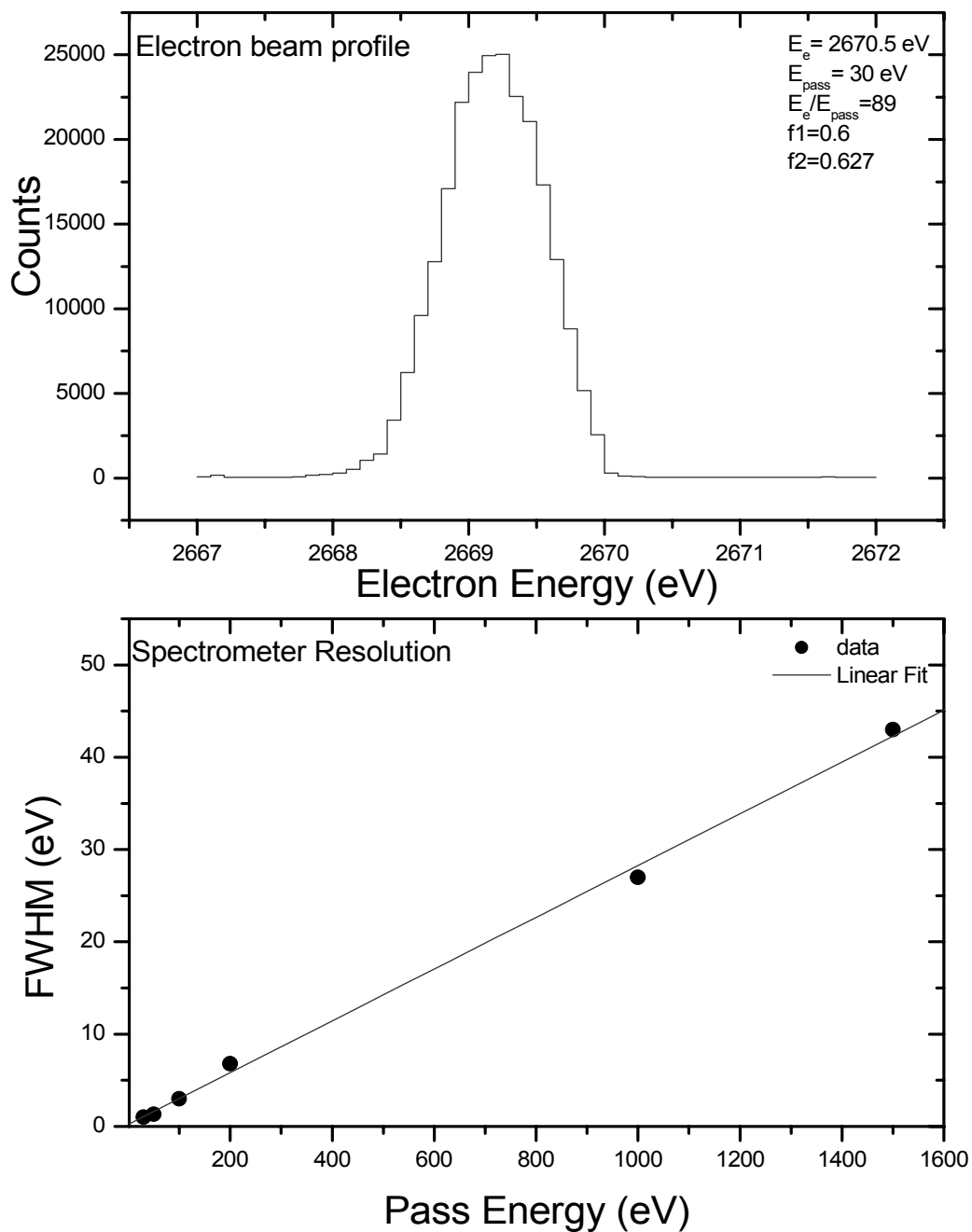


Figure 8 The top panel shows an electron beam profile resolved by the spectrometer. The full width at half maximum is 0.75 eV. The bottom panel shows the linear dependence of the spectrometer resolution on the pass energy of the electrons.

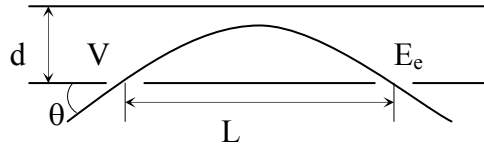


Figure 9 A parallel plate spectrometer and some of its parameters are depicted.

Parallel plate spectrometer	First stage	Second stage
Entrance slit width (w_1)	0.178	0.05
Entrance slit length (h_1)	0.376	0.366
Exit slit width (w_2)	0.124	0.095
Exit slit height (h_2)	0.178	0.372
Slit separation (L)	2.582	2.582
Plates separation (d)	0.774	0.774
Spectrometer constant (f)	0.599	0.599
Measured spectrometer constant (f)	0.6	0.627
Energy resolution (R)	0.585	.0281
Copper Grid Transmission	0.9	0.9

Table 2 Design parameters for the two stages of the spectrometer. The spectrometer constants and the energy resolutions are pure numbers. The rest of the values are in inches.

Chapter Three

Zero Degree Electron Spectroscopy

Collision kinematics

In this chapter the zero degree electron spectroscopy for the determination of electron-ion collision cross sections is discussed. The zero degree designation refers to the observation of electrons that are scattered in the same direction as the ions colliding with them in the scattering chamber. After the collision of ions with the target electrons, the electrons are scattered in every possible direction. However, for the purpose of resonant electron capture and release of electrons from the ions (i.e. electrons emitted from projectile ions), the zero degree angle of observation offers the best possible choice since the kinematic broadening is kept to a minimum [48]. At other angles of observation these resonant lines may be obscured due to the kinematics of ion-electron collisions.

The collision kinematics of the scattering process is best understood when the momenta of the electron and the much heavier projectile ion in the collision are depicted in the laboratory frame of reference. In this reference frame after the collision the electron will have gained the momentum of the projectile in addition to its momentum [54]. The final magnitude of the electron momentum is determined with the use of the cosine law of addition in a triangle:

$$\vec{v} = \vec{v}' + \vec{V} \quad (3.1)$$

$$v^2 - 2vV \cos \theta + (V^2 - v'^2) = 0 \quad (3.2)$$

$$v = V \cos \theta \pm \sqrt{v'^2 - V^2 \sin^2 \theta} \quad (3.3)$$

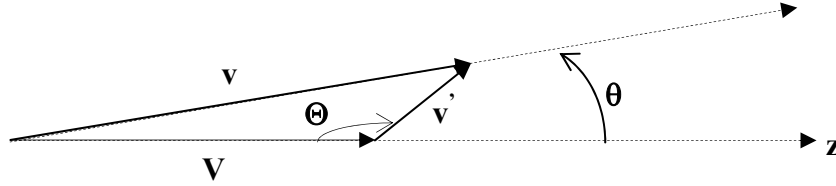


Figure 10 The velocity of the scattered electron in the laboratory frame of reference, v , is determined by the addition of the electron velocity in the projectile frame, v' , to the velocity of the projectile V . z is the direction of zero degree observation. θ is the angle of scattering in the laboratory frame of reference. Θ is the angle of scattering in the projectile frame.

Figure 10 shows the relationship between the angle of scattering in the laboratory and the velocity of the electron in the projectile frame of reference. Beyond a certain critical angle, $\theta_c = \sin^{-1}(\frac{v'}{V})$, electrons of energy $E' = 0.5v'^2$ are no longer detected. This implies that electrons with velocities smaller than the projectile velocity are scattered in the forward direction. Electron energies associated with these velocities are (in a.u.):

$$E = \frac{1}{2}v^2, \quad t = \frac{1}{2}V^2, \quad E' = \frac{1}{2}v'^2 \quad (3.4).$$

Rewriting the velocity formulas in terms of the energies results in

$$\sqrt{E} = \sqrt{t} \cos \theta \pm \sqrt{E' - t \sin^2 \theta} \quad (3.5).$$

At zero degree observation angle

$$E = (\sqrt{t} \pm \sqrt{E'})^2 \quad (3.6).$$

The cusp energy, t , is the energy of the electrons traveling at the same speed as the projectile. A kinematic broadening of the electron spectrum occurs due to the acceptance angle of the spectrometer, $\Delta\theta$, and the observation angle of the spectrometer, θ , relative to the collision. The acceptance angle of the spectrometer is defined by the exit slit of the second stage and is 0.6° (0.01 radians). The first order term in a Taylor expansion of equation (3.5) about $\theta = 0$ vanishes. The second order term results in:

$$\left(\frac{\Delta E}{E}\right)_{\theta=0} = \sqrt{\frac{t}{E'}}(\Delta\theta)^2 \quad (3.7).$$

For electron scattering resonances t is tuned to match E' . As a result the energy broadening is 10^{-4} of the electrons' lab energy.

Experimental setup

The J R Macdonald Laboratory's EN tandem Van de Graaff is used to accelerate negative ions produced at a sputter ion source toward the center of the accelerator. The accelerator terminal at the midsection of the accelerator may maintain a voltage of up to seven megavolts. The ions are stripped of their electrons at this point as they go through an oxygen (or nitrogen) stripping gas. The newly created positive ions accelerate away from the positively charged center and arrive at the exit of the accelerator with an energy of $(q+1)*V_{\text{terminal}}$ MeV. The beam of ions may further be stripped of electrons with the use of foil strippers after leaving the accelerator. These ions also may further be

accelerated through the superconducting linear accelerator (LINAC) and then diverted to the experiment chamber (Figure 11). A rough estimate of the number of resonators required to accelerate the ions to the required energy is determined through the following formula [55]:

$$\Delta E = nq\varepsilon_a L F_v \cos \phi \quad (3.8).$$

In this formula n is the number of resonators, q is the charge of the projectile ion, ε_a is the average acceleration field (up to 3 MeV/m), L is the resonator length, F_v is the transit-time factor, and ϕ is the phase relative to the peak of the acceleration curve. The LINAC is equipped with two types of resonators that are distinguishable by the length of the resonant cavity. One type is 20 cm long and another is 35 cm long. The 20 cm long resonators are capable of a maximum boost in energy when the ion velocity is 0.06β as opposed to the 0.105β for the 35 cm long resonators (see Table 3). These are referred to as low β and high β resonators respectively.

$\beta=V/c$	L (m)
0.06	0.2
0.105	0.35

Table 3 Length of resonators and the maximum amount of boost they can provide.

For example, in order to produce a $68 \text{ MeV } Mg^{11+}$, the energy needed to observe $3\ell 3\ell'$ resonances in this ion (see chapter five), the ions are passed through the Van de Graaff accelerator set at six megavolts to produce a Mg^{5+} beam of 36 MeV . The highest fraction of Mg^{11+} is produced by post-stripping the $36 \text{ MeV } Mg^{5+}$ ions. This fraction is

equal to 0.76. For $\phi = 0$ and a transit time factor close to one, five low beta resonators, $\beta \approx 0.06$, are sufficient. (There are twelve low beta and four high beta resonators in the LINAC.) To add the additional 32 MeV required, the beam is pre-bunched to a 1 ns time width prior to its entrance to the Van de Graaff accelerator and super-bunched to 100 ps prior to its entrance to the LINAC. The beam may be re-bunched at the exit of the LINAC so as to have a sharp peak at the desired energy.

Four-jawed slits and quadrupole magnets are used to trim and focus the beam before delivery into the collision chamber. Inside the chamber the ions are collided with the target gas. The ions then exit through a hole at the back plate of the first stage of the spectrometer and are collected by a Faraday cup. These ions are recorded with a current integrator in order to calculate their electron yield. The electrons scattered at zero degrees are deflected at the first stage by an analyzing voltage and directed to the second stage. The electrons may be decelerated between the two stages by application of a retardation voltage. A passing voltage at the second stage directs the analyzed electrons toward the channel electron multiplier. The channeltron is electrically isolated from ground in the case of high resolution spectroscopy in order for the electrons to arrive with a constant passing energy regardless of the incoming electron energy, E_e (see Figures 12 and 13). The schematics shown in Figure 12 and Figure 13 are for high energy resolution detection mode (the deceleration mode) and for constant electron energy detection. For low energy resolution detection mode (the no deceleration mode) the front plate of the second spectrometer is grounded and the HP power supplies are no longer isolated from the ground.

Figure 11 A schematic of the experimental setup: the ions are accelerated in the Van de Graaff accelerator and the LINAC to the required energy. The ions are then directed to the collision chamber.

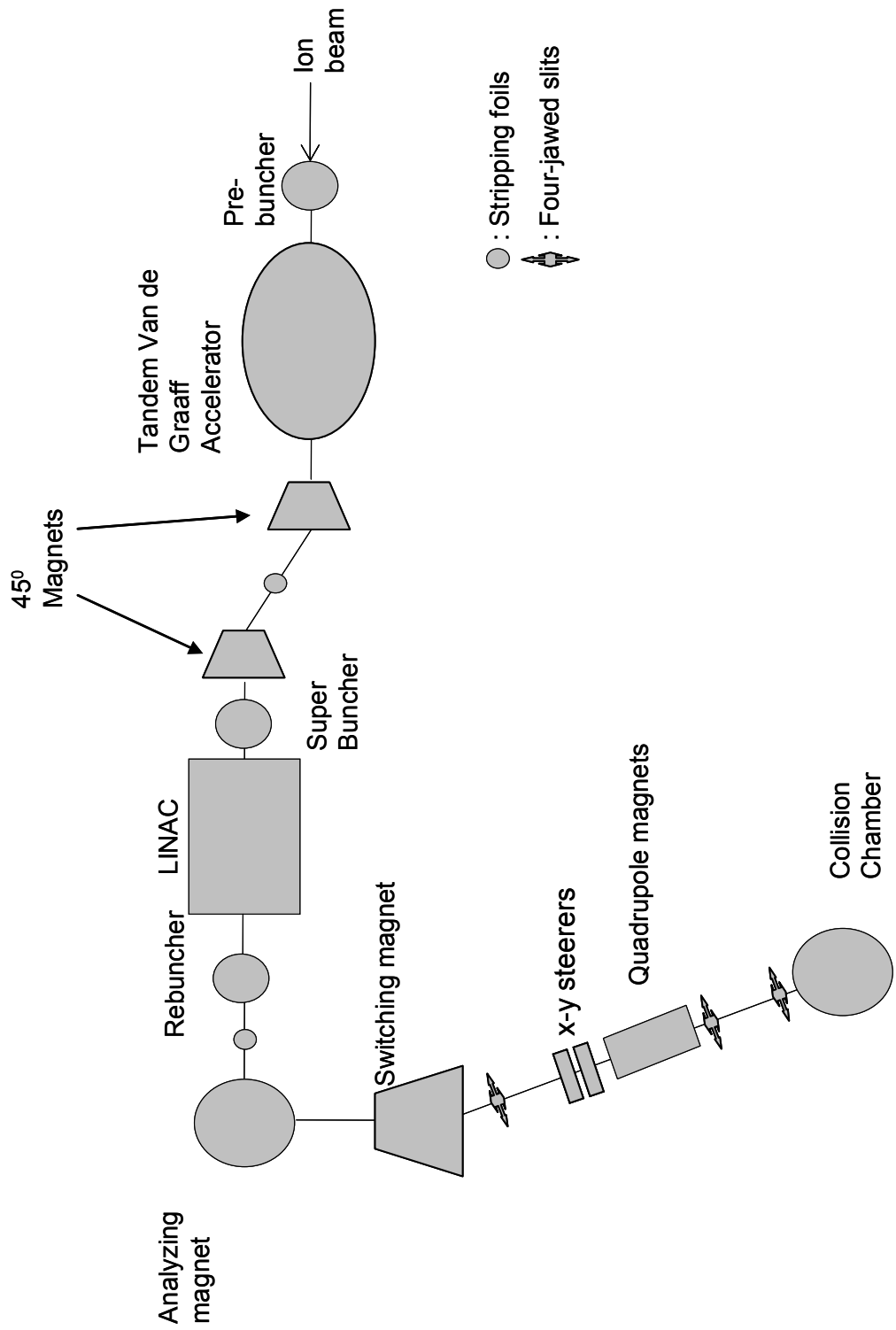


Figure 12 A schematic of applied voltages to the double parallel plate spectrometer is depicted. All energies are in units of eV. After the collision with the target the ions are collected at the Faraday cup (FC). The zero degree scattered electrons are deflected through the two stages of the spectrometer and collected by the channel electron multiplier (CEM). In the low resolution mode V_R is grounded.

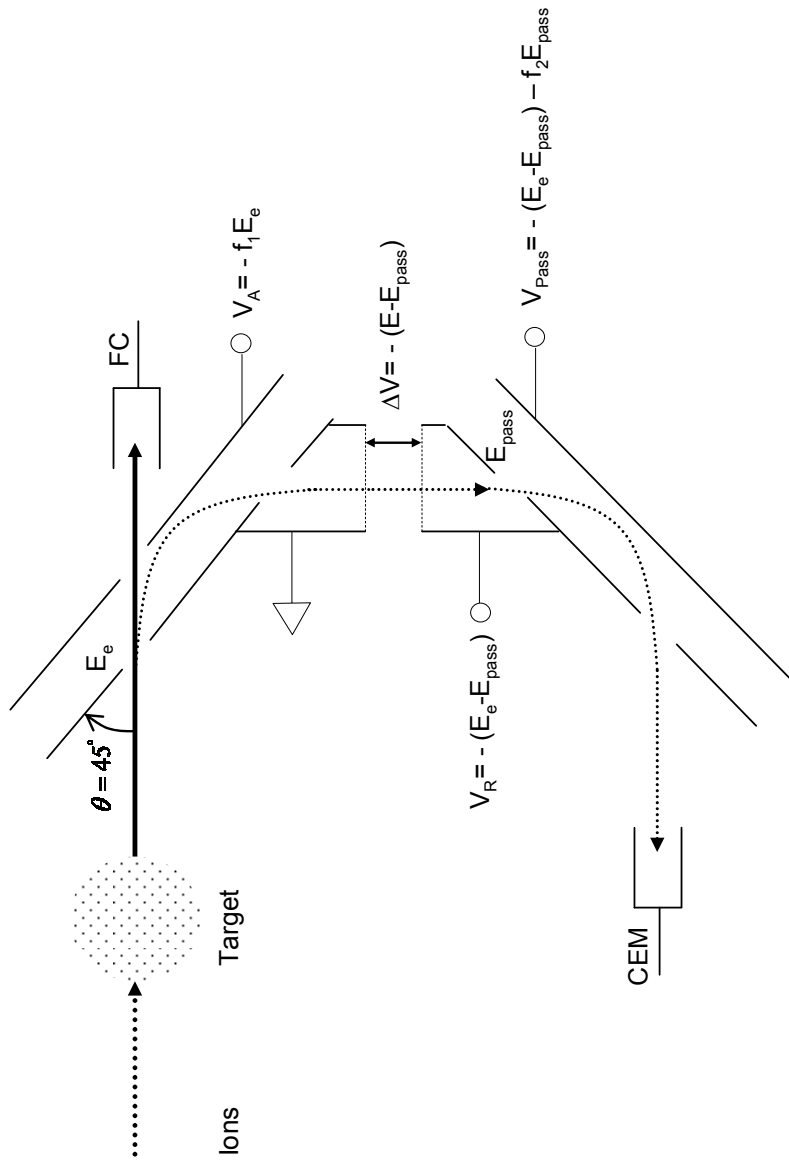
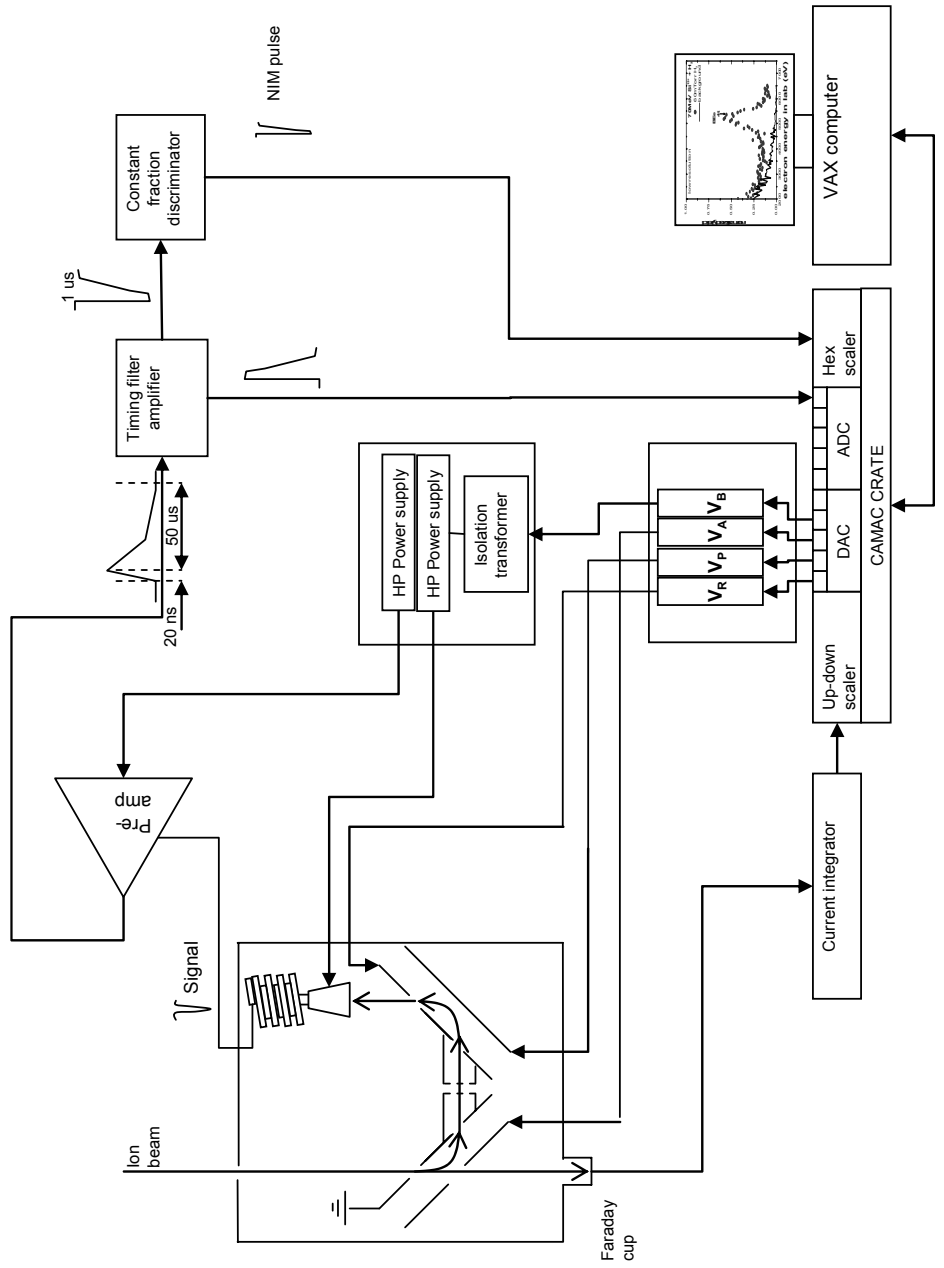


Figure 13 A schematic of the electronics set up for the experiments. The HP power supplies are isolated from the ground so that they may be floated to high voltages by the CANBERRA solid state 10 kilovolt power supplies (labeled V_R , V_p , V_A and V_B). A one to one isolation transformer is used; otherwise, the CANBERRA power supplies load the circuit. The ADC is used at times to monitor the pulse height distribution from the channel electron multiplier.



Chapter Four

Preliminary test experiments

Experiments with boron, silicon and fluorine ion beams were performed to test the abilities of the spectrometer. Experiments were done with B^{2+} and B^{4+} ion beams to investigate the possibility of observing high energy electrons produced by the Fermi shuttle scattering of electrons from ions [56, 57]. Fermi shuttle electrons are electrons caught in the combined field of the projectile ion and target ion. These electrons can undergo several elastic scatterings leading to a series of electrons with velocities of $1v$, $3v$, $5v$, etc if they originate from the projectile and $2v$, $4v$, $6v$, etc if they originate from the target. Figure 14 exhibits the ability of the spectrometer to deflect and detect electrons up to 12 keV in energy. However above about 4 keV an unexpected steady rise in the cross section is seen. This is believed to be due to rescattered electrons finding their way to the detector. Experiments with silicon also showed a high level of background that could be explained as the result of rescattered electrons entering the spectrometer from outside the collision region (Figure 15 and Figure 24).

Since the background levels in the spectra were high and since at high voltages a steady increase in the number of background electrons was observed, some modifications were made to the spectrometer assembly. The deflector plates were sanded to remove sharp edges and corners that may have caused sparking. All electrical sockets on the

plates were removed and the resistors were soldered directly to the plates. Care was taken that all soldered parts made smooth surfaces. A brass shielding was made for the spectrometer to separate it from the rest of the equipment in the chamber and from all sources of rescattered electrons within the chamber.

Following these modifications electron spectra of hydrogen-like fluorine colliding with a hydrogen target gas were taken and the binary encounter electron peak (BEe peak) and the $(2p^2)^1D$ resonant peak were observed at various resolutions. The binary encounter electrons are electrons elastically scattered from the projectile ion. These electrons travel at about twice the velocity of the projectile ($\sim 2V$) at zero degrees in the laboratory frame. By setting $v' = V$ and $\theta = 0^\circ$ in equations 3.1 and 3.5 to and it can be seen that, $v = 2V$ and the BE electrons have an energy of about four times the cusp electrons ($E \approx 4t$). Due to the Compton profile of the electrons, v' has a distribution of velocities in the projectile frame of reference. In the laboratory frame of reference the electrons velocities, v , are above and below the value of V ; therefore, in the laboratory frame of reference the BE electron peak is seen to have a wide range in energy. Figure 16 shows the BE electron peak and $(2p^2)^1D$ resonant elastic scattering peak of fluorine at low and high resolutions. The error bars on the data points are due to counting statistics. The dash dotted lines are the calculated enhanced classical Rutherford cross section for scattering folded with the electron momentum profile of the hydrogen molecule [58]. The solid black lines are the theoretical calculation of the resonant peak folded with the spectrometer's response function [59]. The spectrometer's response function is assumed

to be a normalized Gaussian with a full width at half maximum equivalent to the energy resolution of the second stage of the spectrometer.

Calculation of cross sections from experimental results

The number of electrons collected in the scattering experiments is directly related to the cross section for such collisions. This relation is

$$N_e = N_i \cdot n_T \cdot \ell \cdot \Delta\Omega \cdot R \cdot E \cdot \varepsilon_D(E) \cdot \frac{\partial^2 \sigma}{\partial \Omega \partial E} \quad (4.1).$$

In this formula N_e is the number of electrons detected, N_i is the number of incident ions on the target, n_T is the gas target density, ℓ is length of the gas cell, $\Delta\Omega$ is the solid angle the spectrometer subtends at the exit slit of the spectrometer, R is the energy resolution of the spectrometer, E is the energy of the detected electrons, $\varepsilon_D(E)$ is the spectrometer's detection efficiency of the scattered electrons and finally $\frac{\partial^2 \sigma}{\partial \Omega \partial E}$ is the collision cross section differential in the solid angle of the spectrometer and in the analyzing energy.

The number of electrons detected depends on the channeltron detection efficiency and the transmission factor of the copper mesh grids placed between the two stages of the spectrometer. The copper mesh grids have a 90% transmission factor. Two such grids are used to decelerate electrons between the two stages of the spectrometer in high resolution mode. Thus only 81% of electrons can be expected to be transmitted through the

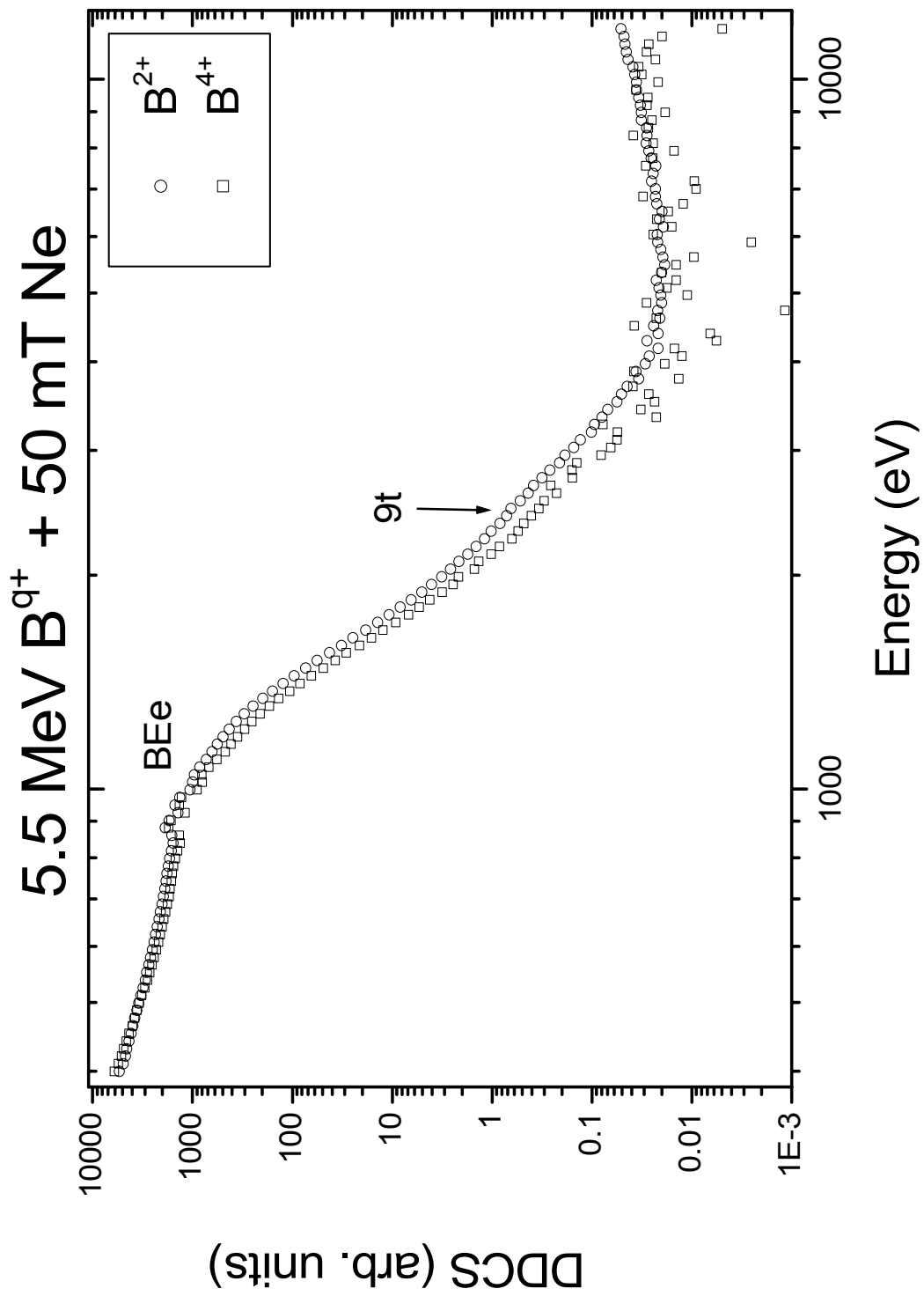
spectrometer and into the channeltron. In high resolution mode the analyzed electrons may diverge in the deflection plane even more compared to the normal mode due to the deceleration they experience between the two stages. Thus the detection efficiency of the spectrometer, $\varepsilon_D(E)$, depends on the detection efficiency of the channeltron and the ability of the spectrometer to transmit the electrons through the two stages and into the channeltron.

The cross section of the binary encounter electron peak is determined by normalizing the electron yield to the known cross section for this peak or to the theoretically determined cross section of the resonance seen at the top of the binary encounter peak. In this way the spectrometer's detection efficiency, $\varepsilon_D(E)$, can be determined. This efficiency varies for different electron energies and pass-energies. As a result this value is changed to obtain the best reasonable fit between theory and experiment. Table 4 shows the detection efficiency calculated from the aforementioned fluorine experiment. Figure 17 shows the spectrometer's transmission tested with an electron gun and the fluorine experiment. The transmission curve at a given initial electron energy was determined by normalizing the area of the electron peak at different pass energies to the area of the electron peak measured at low resolution mode. As expected for the transmission curves overlap and exhibit the $1/F$ behavior.

Pass energy (eV)	$\varepsilon_D(E)$
2440	0.03
400	0.03
200	0.03
100	0.02
50	0.02
25	0.02

Table 4 Detection efficiency for various electron pass energies is tabulated.

Figure 14 5.5 MeV boron ions were collided with Ne gas to investigate the possibility of the production of Fermi shuttle electrons. An increase in the cross section around 4000 eV is due to the rescattered electrons.



70MeV Si¹³⁺ + 60 mT H₂

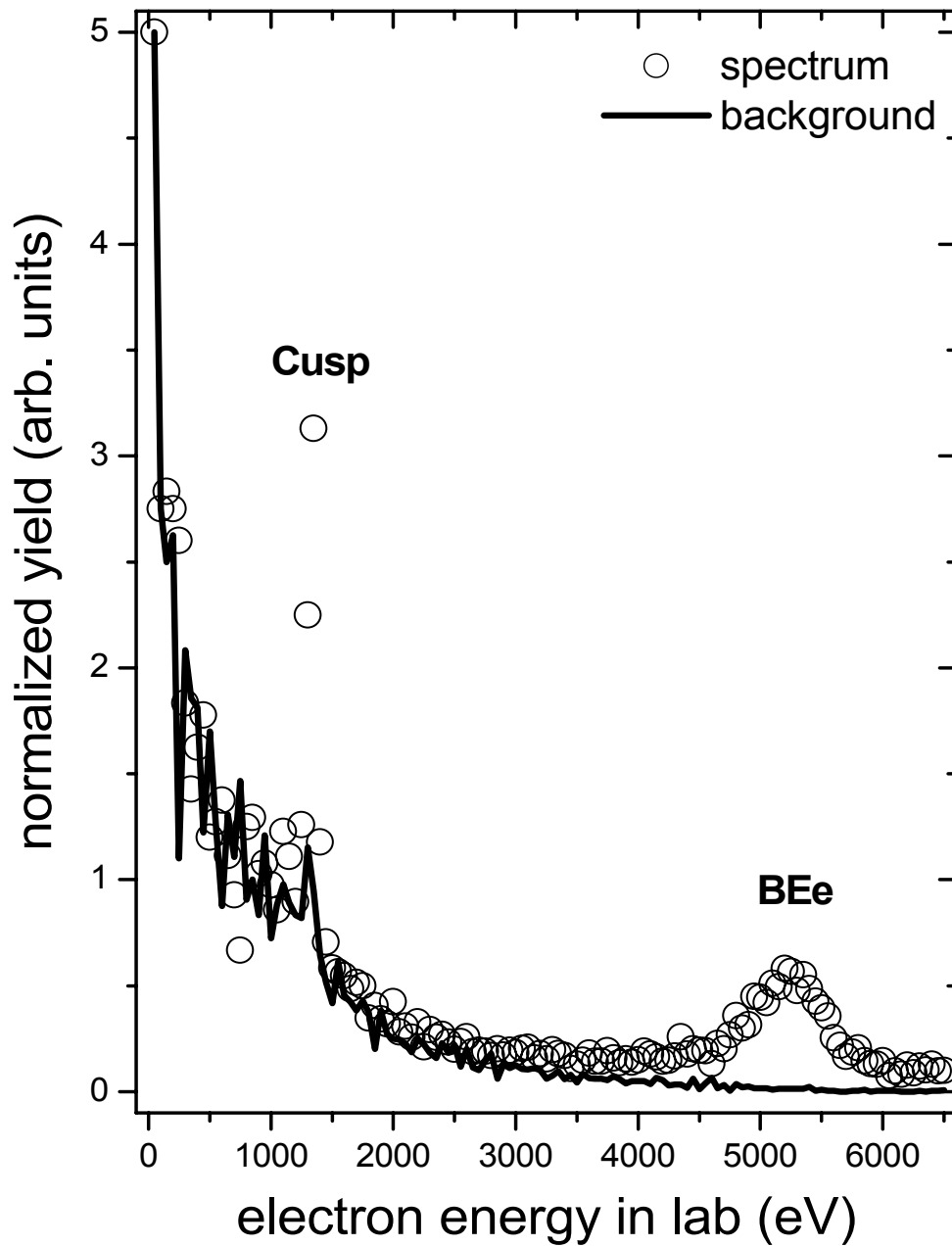


Figure 15 Low resolution electron spectrum of hydrogen-like silicon colliding with a target gas taken at zero degree angle of scattering. The high level of background indicates that electrons from sources other than the ion-target collision find their way through the spectrometer and into the detector.

22 MeV F^{8+} + 30 mT H_2

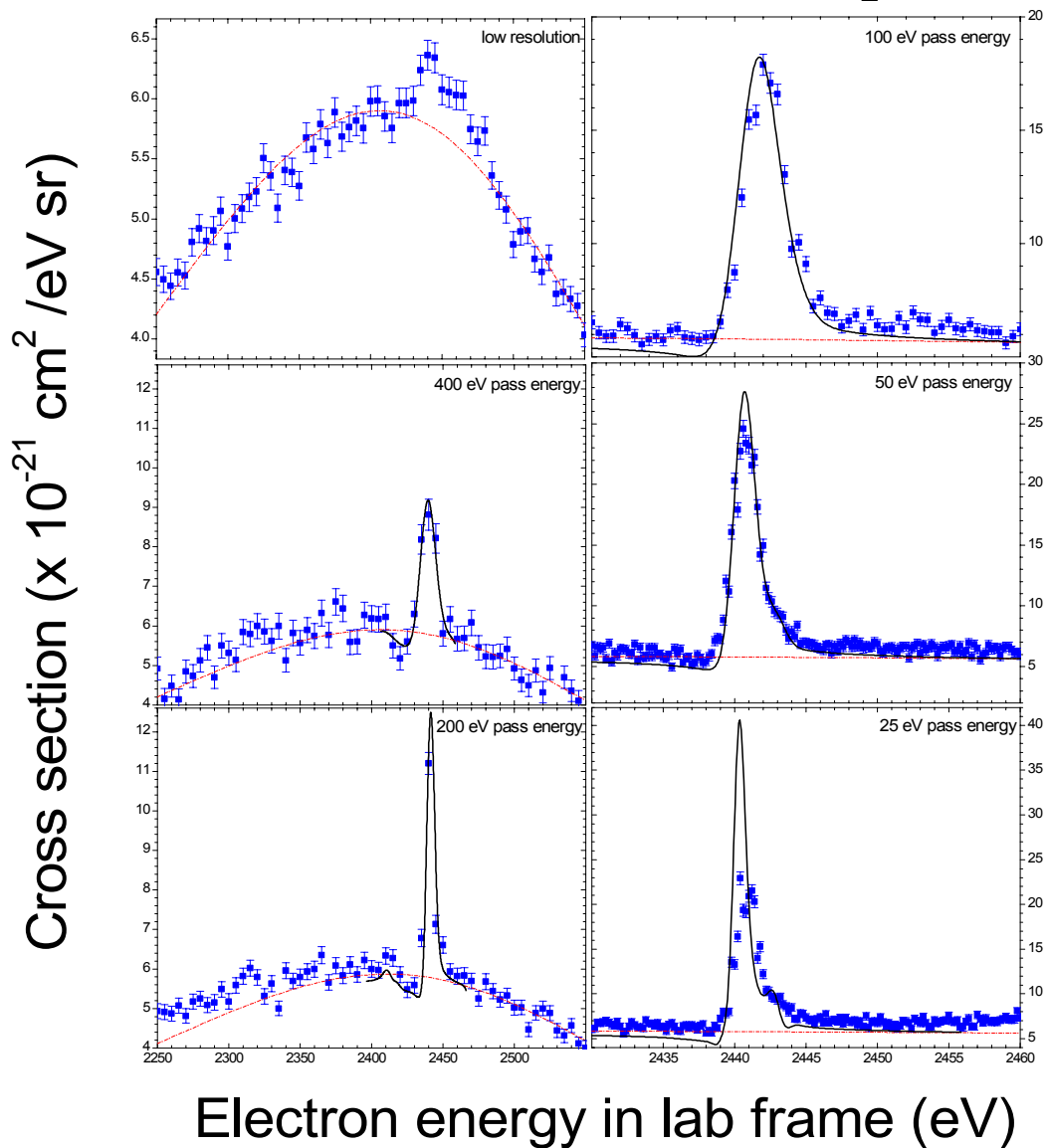
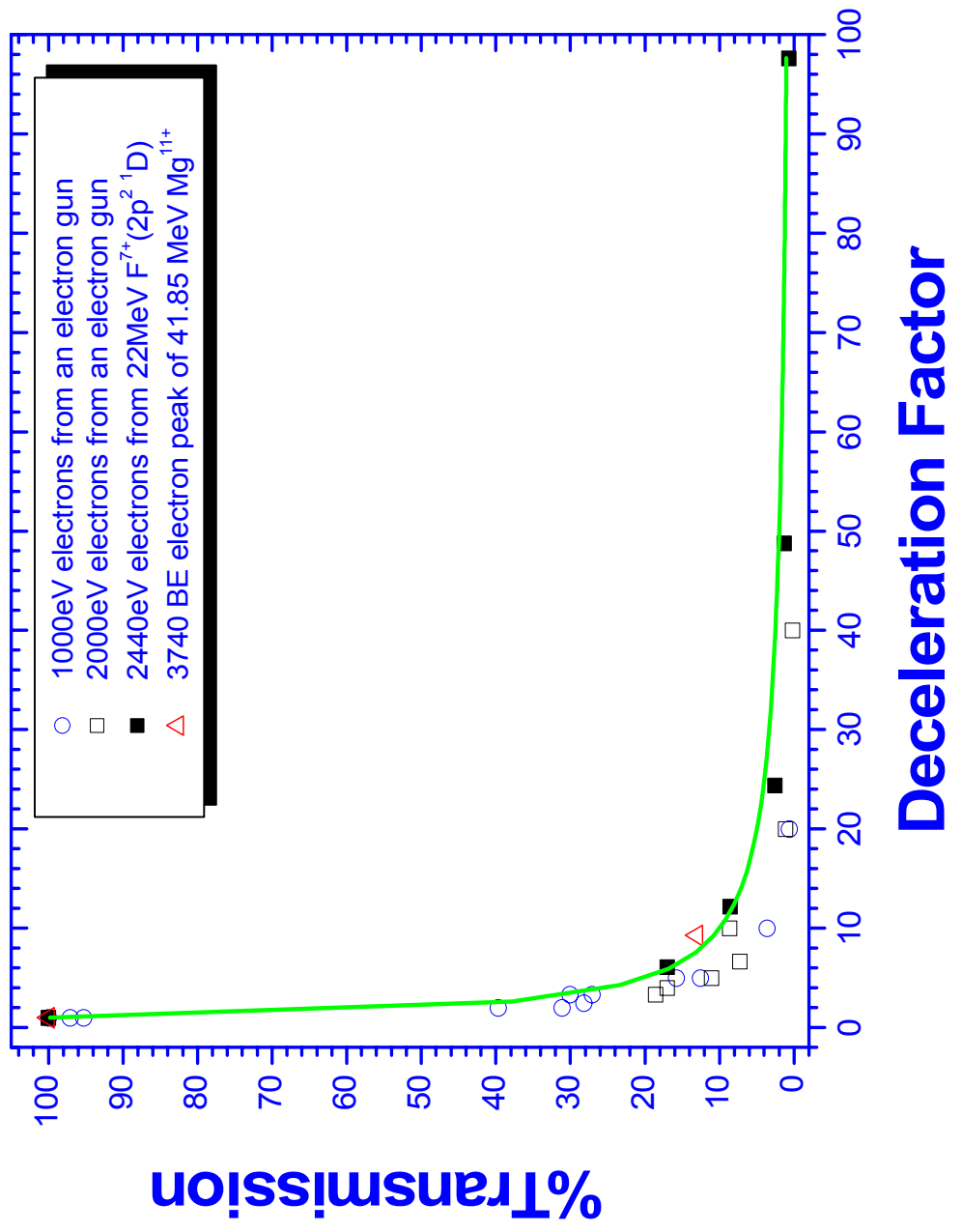


Figure 16 Electron spectra of hydrogen-like fluorine colliding with a hydrogen target gas are depicted. The $2p^2\ ^1D$ line is seen at low resolution on top of the binary encounter peak. At higher resolutions, the peak is seen with a narrower profile. At 25 eV pass energy the peak is no longer as sharp at the theoretical calculation. This may be due to the loss of electrons at this pass energy.

Figure 17 Electron spectrometer transmission is depicted. As expected the transmission curves overlap and exhibit a $1/F$ behavior. The green line is a $1/F$ fit to the fluorine data.



The ability of the spectrometer to deflect energetic electrons is estimated to be limited to 21 keV. This is based upon the assumption that the plates of the spectrometer can withstand at least 1 kilovolt per millimeter of separation without sparking. Each plate of spectrometer is 0.062" from the next plate, and since each stage of the spectrometer has seven equipotential plates the total voltage each stage can withstand is about 12.6 kV. The electron spectrometer has so far successfully analyzed electrons of energies of up to 6500 eV in the silicon experiment (see Figure 15). The actual upper limit of the ability of the spectrometer to analyze energetic electron is yet to be decided. The $2p^2\ ^1D$ resonance has been studied for several hydrogen-like ions colliding with molecular hydrogen gas target [31]. It would be of interest to study this resonance for higher and lower Z ions other than those already studied to get a better picture of the overall trend in the cross section of such collisions. There is limited number of such experiments for high Z ions due to the beam energy required to from these states for high Z ions. Hydrogen-like ions up to silicon can be accelerated through the J. R. Macdonald Laboratory's Tandem Van de Graaff accelerator and the LINAC to achieve the energies needed for $2p^2\ ^1D$ state.

Figure 18 shows the possible ions that may be collided with a target gas to produce a doubly excited helium-like $2p^2\ ^1D$ state from the hydrogen-like ground state of these ions if the spectrometer is indeed capable of analyzing 21 KeV electrons. This figure only illustrates the BE electron peaks corresponding to the energies required to excite this resonance state.

Figure 19 shows how the ion energy is calculated to match the energy needed to create the doubly excited states. To create the doubly excited states the BE electron peak energy is matched to the excitation energy from the ground state of the ion to the doubly excited autoionizing state. For example, in order to create a $2\ell 2\ell'$ state from the Mg^{11+} ion, beam energy of 42 MeV is needed, and to create a $3\ell 3\ell'$ state from the Mg^{11+} ion the beam energy needed is 68 MeV. A simple quantum defect model for the doubly excited state is used to calculate these energies:

$$E_{n,n'} = -\frac{Z'^2}{2} \left(\frac{1}{n^2} + \frac{1}{n'^2} \right) \quad (4.2)$$

In this formula $Z' = Z - 0.3$ and $n = n'$.

Figure 18 The calculated binary encounter electron cross sections for different ions are demonstrated. The spectrometer is nominally capable of analyzing energetic electrons of up to 21 keV. The peak of the binary encounter electrons corresponds to the energy required to create a doubly excited $2p^2$ state from the ground state of the hydrogen-like ions. In the projectile frame the binary encounter electrons correspond to Rutherford scattering.

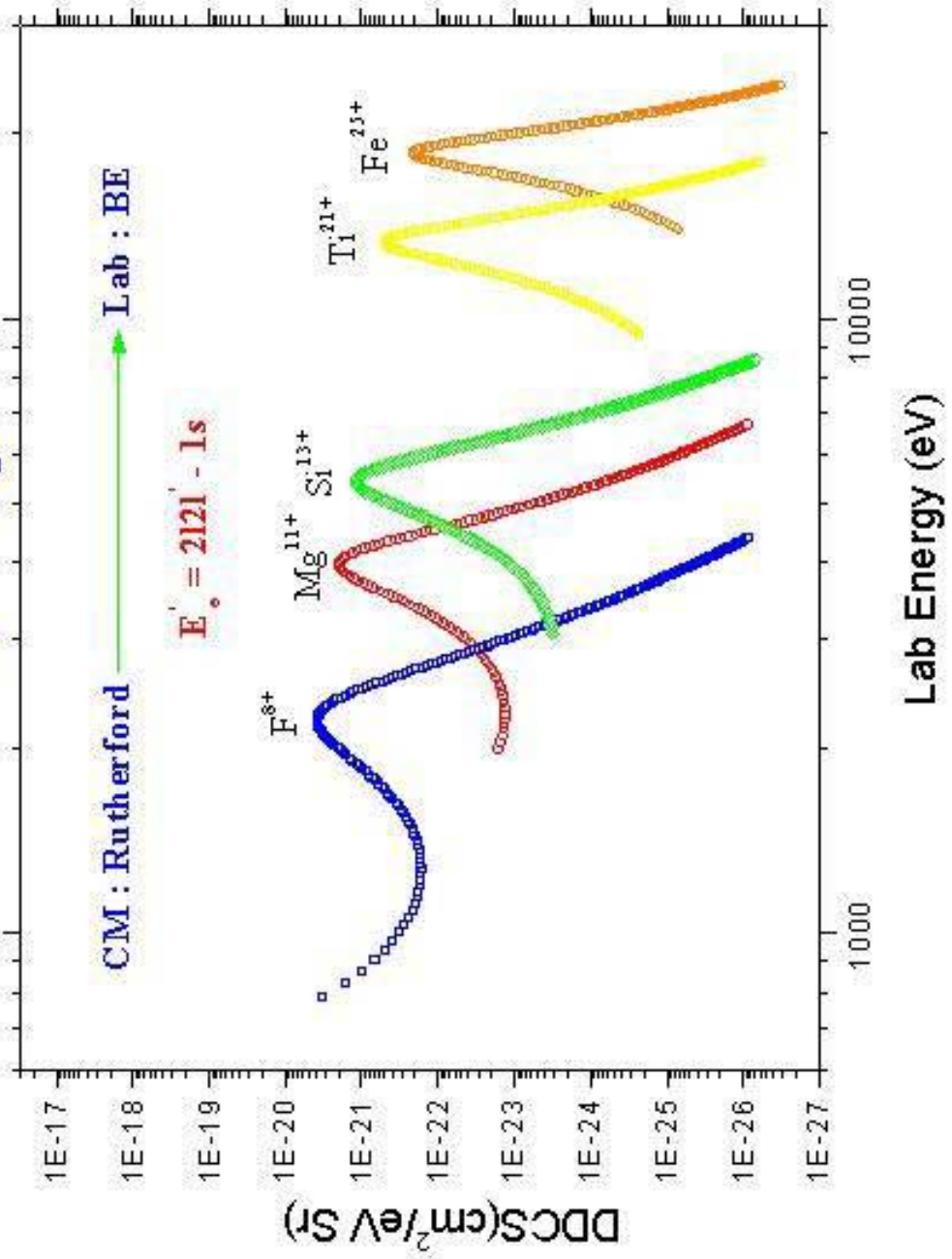
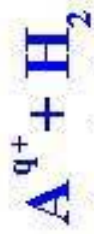
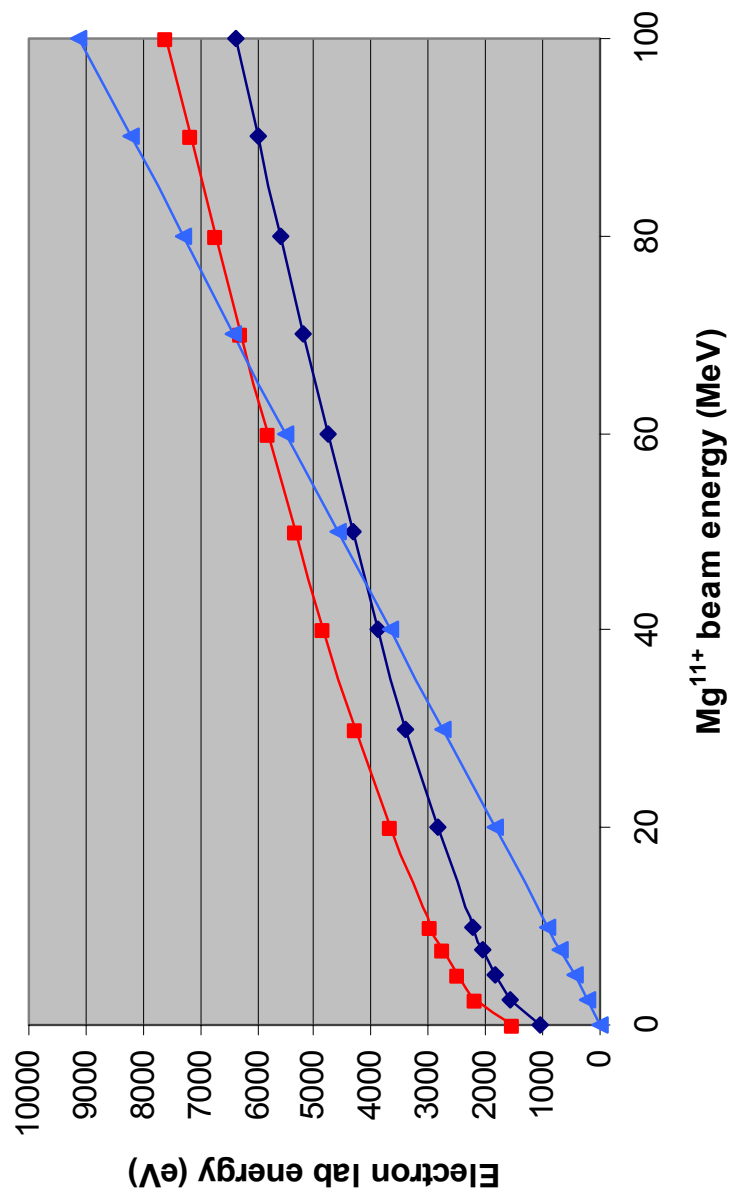


Figure 19 The BEE peak is matched to the Auger energy of the electrons decaying from the doubly excited state of the ion to the ground state in order to create the doubly excited states. For a $2\ell 2\ell'$ doubly excited state, the Mg^{11+} ion energy needed is 42 MeV. Similarly for a $3\ell 3\ell'$ doubly excited state, the Mg^{11+} ion energy needed is 68 MeV.

BE electron peak energy vs Auger energies



—◆— 1s->2|2|' excitation energy (eV) —■— 1s->3|3|' excitation energy (eV) —▲— BE electron peak (eV)

Chapter Five

Experiments with boron, fluorine, magnesium and silicon

These experiments were performed to study the resonance elastic and inelastic scattering mechanisms in collisions of hydrogen-like ions with a thin molecular hydrogen gas target. The experiments with boron were conducted with $5.5\text{MeV } B^{4+} + 20\text{ mT } H_2$. The intensity of the ion beams were on the order of one nano-amperes which made the experiment for resonance inelastic scattering particularly difficult. Data on the resonance elastic scattering from the boron were also collected from these experiments. The electrons scattered at zero degrees were decelerated to pass energies ranging from 25eV to 400 eV in order to get the needed resolution to observe the resonant spectra. Similar pass energies were selected for the experiments with magnesium and silicon ions. For magnesium spectra the ions were first accelerated through the Tandem van De Graaff accelerator and stripped to a medium charge state, then post stripped before the LINAC accelerator and post stripped again after being accelerated through the LINAC to a final charge state of 11+. The ion beam intensity in these experiments was too weak to observe the resonant inelastic scattering spectra for magnesium. Therefore only resonant elastic scattering from the $2\ell 2\ell'$ states of the ion was studied. The resonant excitation strength for this resonance was extracted along with resonant excitation strength for the similar processes in B^{4+} and F^{8+} , and the results were compared to previous experimental results.

The silicon ions were also accelerated through the Tandem and the LINAC accelerators. In the case of silicon the beam intensities were too low to even observe the more prominent spectra of the $2\ell 2\ell'$ resonances. The BE electron peak for Si^{12+} and Si^{13+} were observed and their relative enhancement in the cross section compared to the bare silicon ion was determined. The cross-section enhancement of the BE electron peak for boron and magnesium ions were also determined. The results of these experiments are presented in the following sections.

Impulse approximation method and the electron scattering model

The impulse approximation method is used to relate the obtained electron spectrum from an ion-atom collision to an electron-atom collision experiment. The central theme of this procedure is the assumption that the interaction of the quasi-free target electrons with the projectile can be used to extract the pure electron-projectile ion collision scattering amplitude. This has been a point of misunderstanding in the physics community for some years since the process has been studied experimentally. There is overwhelming evidence in the literature that has demonstrated that the cross section for the binary encounter electrons in high velocity collisions $V_p \gg \langle v_e \rangle$, where $\langle v_e \rangle$ is the average orbital velocity of the quasi-free bound electrons, is given to an extremely high accuracy by the elastic potential scattering of free electrons from the projectile [33,44,58,64-69]. Furthermore, the cross section for the production of Auger electrons emitted from doubly excited states agrees well with the predicted cross section for resonance plus non-resonance amplitudes for elastic scattering of a free electron from the

projectile ion [19, 20, 31, 44-60]. These resonance peaks in the electron spectra exhibit an interference pattern expected from such a two amplitude process. The non-resonance amplitude produces the binary encounter electrons. The resonance amplitude produces the doubly excited resonance states.

Electron-ion collision experiments are currently very difficult to perform since the beam intensities of the electrons and the ions are relatively weak for a crossed beam or a merged beam experiment. Electron scattering from electron-ion crossed beam experiments have been observed for a few collision systems, but only for a limited number of charge states and a limited number of collision energies [70-76]. No direct measurement of resonance states have been observed by this method. Experiments in which the change in the charge state of the ions have been observed measure the total yield of the ions directly or by observing the x-ray emission from the doubly excited state formed during dielectronic recombination [77]. These types of results are obtained from ion sources such as the EBIS at KSU [26] or EBIT at the Lawrence Livermore National Laboratory [78]. Extremely high resolution total cross sections have been obtained from electron-ion merged beams in ion storage rings such as the CRYRING in Stockholm [79] and the Test Storage Ring at the Max Planck Institute in Heidelberg [80, 81].

In order to study the electron resonances by quasi-free electron projectile ion scattering, the ions are directed to a target atom. The target atom is used as a reservoir of electrons. The loosely bound electrons on a target atom have a range of momenta associated with them. The impulse approximation method assumes that this range of

momenta remains undisturbed by the incoming ion. In the rest frame of the projectile the momentum of the projectile is added to the momentum of the electron to give its final momentum (see Figure 20):

$$\vec{P} = \vec{p}_0 + \vec{p} \quad (5.1)$$

In the electron scattering model the components of \vec{p} in a direction perpendicular to the direction of the ion are ignored. As a result we have:

$$P \approx p_0 + p_z \quad (5.2)$$

The electron energy in this frame is

$$E_e \approx \frac{P^2}{2m} - E_I \quad (5.3)$$

p_z is the bound electron, p_0 is the electron momentum relative to the projectile, E_I is the target electron binding energy and E_e electron energy relative to the projectile.

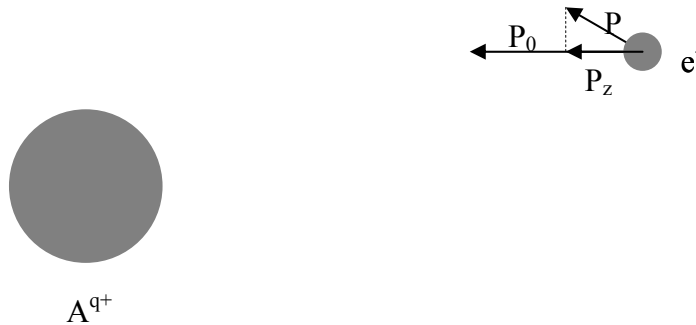


Figure 20 Kinematics of a target electron in the projectile rest frame is depicted. The electron is considered quasi-free if the momentum distribution of the target electron is much less than the projectile laboratory frame velocity. The momentum of the electron in the projectile rest frame is the sum of its momentum due to its bound state in the target and its relative momentum with respect to the projectile.

Since the differential cross section in an electron-ion collision, $\frac{d\sigma(E_e)}{d\Omega}$, is dependent on the incoming electron energy, the differential cross section in an ion atom collision, $\frac{d\sigma(E_e)}{d\Omega}$ needs to be folded with the momentum distribution of the target electron. In the case of a target with electrons from multiple shells or subshells participating in the collision we have:

$$\frac{d\sigma}{d\Omega} = \sum_i \int \frac{d\sigma(E_{e_i})}{d\Omega} |\Psi_{e_i}(E_{e_i})|^2 dE_i = \sum_i \int \frac{d\sigma(P_i)}{d\Omega} |\Psi_{e_i}(\vec{P}_i)|^2 d^3\vec{P}_i \quad (5.4)$$

The Compton profile of a target electron is defined as

$$J(p_{z_i}) = \int_{-\infty}^{+\infty} \int_{-\infty}^{+\infty} dp_{x_i} dp_{y_i} |\Psi_{e_i}(\vec{P}_i)|^2 \quad (5.5)$$

$J(p_{z_i})$ is the probability density of a target electron having momentum p_{z_i} . $\Psi_{e_i}(\vec{P}_i)$ is the target electron's wave function in momentum space. In the case of the interaction of the ion with multiple target electrons, the contribution from all the electrons needs be considered. The experimentally determined Compton profiles for H₂ and He are determined by equation 5.6 with the parameters given in Table 5 [82].

$$J(p_z) = \sum_{n=1}^m \frac{a_n}{\left[1 + \left(\frac{p_z}{\xi_n}\right)^2\right]^{n+2}} \quad (5.6)$$

Hydrogen molecule			Helium atom		
n	a _n	ξ _n	n	a _n	ξ _n
1	1.0012	0.9896	1	-0.0957	2.1828
2	0.5383	1.5566	2	0.0514	4.1598
			3	0.1342	3.5200
			4	0.7316	2.3948
			5	0.2426	1.5732

Table 5 Compton profile parameters for the hydrogen molecule and the helium atom.

With the use of equations 5.2, 5.3, 5.4 and 5.5 the cross-section of the quasi-free electron doubly differential in energy and solid angle (DDCS) in the center of mass is obtained:

$$\frac{d^2\sigma}{dEd\Omega} = \frac{d\sigma(E_e)}{d\Omega} \cdot \frac{J(p_z)}{V_p + p_z} (a.u.) \quad (5.7)$$

The DDCS in the lab frame can be obtained by transformation [83, 84]:

$$\frac{d^2\sigma}{dE_L d\Omega_L} = \sqrt{\frac{E_L}{E_e}} \frac{d^2\sigma}{dEd\Omega} \quad (5.8)$$

Determination of RTEA scattering cross sections

Resonant transfer and excitation (RTE) is a process where an electron from the target is captured by the projectile at the same time a projectile electron is excited to a higher level. This process in the projectile rest frame is similar to the resonance process of radiationless capture (Feshbach resonance) of an electron impinging on the ion. In the RTE process, however, the momentum profile of the bound target is folded into the overall cross section of the collision. The impulse approximation (IA) technique takes into account the initial momentum distribution of the target electron by assuming that the initial state of the bound target electron remains undisturbed during the collision. An RTE is either followed by Auger decay (RTEA) or by the emission of a photon (RTEX) [77, 85]. Similar counterparts of RTEA and RTEX exist in electron-ion collisions. In the case of electron-ion scattering the Auger decay process is known as resonant excitation scattering (RES), but if autoionization becomes impossible after the x-ray emission the process is known as dielectronic recombination (DR) [86-90].

Resonant elastic scattering

Single differential scattering cross sections (SDC) for electron-ion collisions can be calculated with the formulation given by Griffin and Pindzola [61, 62]. For the case of elastic scattering of an electron from the ground state of an ion the SDC can be written as follows:

$$\frac{d\sigma_{if}}{d\Omega} = \frac{d\sigma_{if}^{Coul}}{d\Omega} + \frac{d\sigma_{if}^{int}}{d\Omega} + \frac{d\sigma_{if}^{SR}}{d\Omega} \quad (5.9),$$

$$\frac{d\sigma_{if}^{Coul}}{d\Omega} = \delta_{if} \frac{\left(\frac{q}{k_i}\right)^2}{4k_i^2 \sin^4\left(\frac{\theta}{2}\right)} \quad (\text{Rutherford Term}) \quad (5.10),$$

$$\begin{aligned} \frac{d\sigma_{if}^{int}}{d\Omega} = & -\delta_{if} \frac{\left(\frac{q}{k_i}\right)}{4(2S_i+1)k_i^2 \sin^2\left(\frac{\theta}{2}\right)} \quad (\text{Interference term}) \\ & \times \text{Im} \left[e^{-i\left(\frac{q}{k_i}\right)\ln\left[\sin^2\left(\frac{\theta}{2}\right)\right]} \sum_S (2S+1) \sum_{\ell=0}^{\ell_{\max}} (2\ell+1) P_{\ell}(\cos\theta) e^{2i\left[\sigma_{\ell}\left(\frac{q}{k_i}\right) - \sigma_0\left(\frac{q}{k_i}\right)\right]} T_{S\ell\ell}(i \rightarrow f) \right] \end{aligned} \quad (5.11),$$

$$\begin{aligned} \frac{d\sigma_{if}^{SR}}{d\Omega} = & \frac{1}{8(2S_i+1)k_i^2} \sum_{\ell, \ell'=0}^{\ell_{\max}} (2\ell+1)(2\ell'+1) \sum_S (2S+1) \sum_{\lambda=|\ell-\ell'|}^{\ell+\ell'} (2\lambda+1) \begin{pmatrix} \ell & \ell' & \lambda \\ 0 & 0 & 0 \end{pmatrix}^2 P_{\lambda}(\cos\theta) \\ & \times e^{i\left[\sigma_{\ell}\left(\frac{q}{k_i}\right) + \sigma_{\ell}\left(\frac{q}{k_f}\right) - \sigma_{\ell'}\left(\frac{q}{k_i}\right) - \sigma_{\ell'}\left(\frac{q}{k_f}\right)\right]} T_{S\ell'\ell'}^*(i \rightarrow f) T_{S\ell\ell}(i \rightarrow f) \quad (\text{Short range term}) \end{aligned} \quad (5.12).$$

$\sigma_{\ell}(x) = \arg[\Gamma(\ell+1-ix)]$ is the Coulomb phase shift. $\varepsilon_i = \frac{1}{2}k_i^2$ and $\varepsilon_f = \frac{1}{2}k_f^2$ are the

initial and final electron energies and ℓ and ℓ' are the angular momenta of the incident and scattered electron. For a one electron ion the sum over the total spin is from

$S = 0$ to $S = 1$, and at $\theta = 180^\circ$, $P_{\lambda}(\cos\theta) = (-1)^{\lambda}$. ℓ_{\max} is the maximum partial wave

included in the calculation. The first term is due to the long-range elastic Coulomb

scattering of the electron from the ion. The coherent addition of the Coulomb and short-

range scattering amplitudes produces the interference term in equation 5.12. This term is

responsible for the interference seen between the direct scattering and the resonance

scattering lines seen in elastic scattering. Finally the short-range cross section is generally

due to the polarization of the ion and exchange interaction between the incident electron

and the target electron in the short-range potential. The resonance lines are also due to

this term.

As mentioned earlier the RTE process and direct excitation are two competing processes that cannot be distinguished. As a result the RTE and direct excitation scattering amplitudes interfere. The direction of the incoming electrons in the projectile frame may be taken as the quantization axis of the system. Due to the rotational symmetry of the collision with respect to the direction of the beam, the Auger cross section is only dependent on the magnitude of the magnetic quantum number $|M|$ of the doubly excited atomic state $|SLJM\rangle$.

The selection rules for the Auger decay for resonant excitation scattering from an ion are [43, 91]:

$$\Delta S = \Delta L = \Delta J = \Delta M_S = \Delta M_L = \Delta M = 0 \quad (5.13)$$

$$\Pi_i = \Pi_f \quad (5.14)$$

The quantum numbers and parities refer to the system of ion and the Auger electron.

The rotational symmetry of the collision also results in the angular distribution of Auger electrons symmetric about $\theta = \pi/2$ with the functional form:

$$\hat{W}(\theta) = 1 + \sum_{n=1}^{\infty} A_{2n} P_{2n}(\cos \theta) \quad (5.15)$$

$P_{2n}(\cos \theta)$ are the Legendre polynomials and A_{2n} are the anisotropy coefficients. The magnetic quantum number m_l of the incoming electrons is zero since the axis of

quantization is taken to be in the direction of the incoming beam. Also, the selection rules imply that the magnetic quantum numbers M_l and M_s of the resonant state should match the magnetic quantum number of the initial state of the ion. Thus in RES from the ground state of a hydrogen-like ion to an intermediate doubly excited state the magnetic substate $M_L = 0$. In this particular case $\hat{W}(\theta)$ is simplified to the following form [91, 92]:

$$\hat{W}(\theta) = 4\pi \cdot |Y_{L0}(\theta)|^2 = 2L + 1 \quad (5.16)$$

where $|Y_{L0}(\theta)|$ is a spherical harmonic which corresponds to a doubly excited state $|d\rangle$ with an angular momentum of L .

This rotational symmetry is destroyed in ion-atom collisions due to the interference of the resonance and direct scattering channels in the collision [45, 93-95]. However, assuming the interference between the resonance and direct scattering may be ignored, the resonant excitation scattering strength, Ω_{RES} , may be extracted from the ion-atom collision data. Ω_{RES} is calculated in the LS coupling scheme from the following equation [41, 43, 96]:

$$\Omega_{RES} (cm^2 eV) = \xi_d \cdot \Omega_{RC} = \xi_d \cdot 2.475 \times 10^{-30} \cdot \frac{\omega_d}{\omega_i} \cdot \frac{A_a^{d \rightarrow i} (s^{-1})}{E_a (eV)} \quad (5.17)$$

The radiationless capture strength, Ω_{RC} , is defined by:

$$\Omega_{RC} = \Delta \varepsilon \cdot \bar{\sigma}_{RC} \quad (5.18)$$

Ω_{RC} is a constant compared to the width of the resonance, $\Gamma^{(d)} = \Gamma_a^{(d)} + \Gamma_r^{(d)}$, so long as $\Delta\varepsilon$ is chosen to be large enough. $\bar{\sigma}_{RC}$ is the averaged cross section for radiationless capture over the interval $\Delta\varepsilon$.

E_a is the energy of the Auger transition, and ξ_d , the yield for the Auger decay from the doubly excited state $|d\rangle$ to the state $|i\rangle$, is given by:

$$\xi_d = \frac{A_a^{d \rightarrow i}}{\sum_f A_a^{d \rightarrow f} + \sum_{f'} A_r^{d \rightarrow f'}} \quad (5.19)$$

The sums are over all the possible final states for Auger and radiative transitions. In this formula an A_a indicates an Auger transition rate and an A_r represents a radiative transition rate to a final state. The density of states for this Auger decay is given by $\omega_d = (2L_d + 1)(2S_d + 1)$ for the doubly excited states and $\omega_i = (2L_i + 1)(2S_i + 1)$ for the final states. Of course in the case of resonant elastic scattering the initial and final states of the ion are the same.

To obtain the relationship between the RES cross section and the RC cross section the impulse approximation method is employed [21]. The RTE cross section may be written in the following form:

$$\sigma_{RTE} = \int_{-\infty}^{+\infty} J_i(p_{iz}) dp_{iz} \sigma_{RC}(p_{iz}) \quad (5.20)$$

Assuming the RC cross section is sharply peaked at the value $p = Q$ and that the Compton profile varies slowly, $J_i(p_{iz})$ may be taken out of the integral. Therefore, using

the relationship developed between the momentum and energy (see equations 5.2 and 5.3) we will get:

$$\sigma_{RTE} = \frac{J_i(Q)}{V_p + Q} \cdot \int_{\varepsilon_r - \Delta\varepsilon/2}^{\varepsilon_r + \Delta\varepsilon/2} d\varepsilon \sigma_{RC}(\varepsilon) = \frac{J_i(Q)}{V_p + Q} \cdot \Delta\varepsilon \cdot \bar{\sigma}_{RC} = \frac{J_i(Q)}{V_p + Q} \cdot \frac{\Omega_{RC}}{\varepsilon_0} \quad (5.21)$$

As mentioned earlier $\bar{\sigma}_{RC} = 1/\Delta\varepsilon \int_{\varepsilon_r - \Delta\varepsilon/2}^{\varepsilon_r + \Delta\varepsilon/2} d\varepsilon \sigma_{RC}(\varepsilon)$ and $\Delta\varepsilon$ is taken to equal $\varepsilon_0 = 1a.u.$ energy.

Considering the equations 5.16, 5.17, 5.18 and 5.21 the relationship between Ω_{RES} , the resonant excitation strength, and the differential cross section for RTEA may be written in the following form:

$$\frac{d\sigma^{RTEA}(\Theta = 180^\circ)}{d\Omega} = \frac{J(Q)}{V_p + Q} \cdot \frac{\Omega_{RES}}{\varepsilon_0} \cdot \frac{(2L+1)}{4\pi} \quad (5.22)$$

The motivation to measure the $2p^2^1D$ experiments was to observe any possible enhancement of the interference between directly scattered and resonantly scattered elastic cross sections for the $2p^2^1D$ lines of the hydrogen-like ion colliding with a molecular hydrogen gas target. Previous experiments with lithium-like oxygen and fluorine showed a modest $\sim 3\%$ enhancement in the cross section due to interference [93]. The experiments with boron and magnesium show little change in the contribution of the interference term to the scattering cross section. Figure 21 shows this peak for magnesium taken in high resolution. Theoretically calculated terms of the $2\ell 2\ell'$ manifold can be seen in Figure 22. The measured $(2p^2)^1D$ resonance term can be seen in Figure 23 along with the theoretical calculation convoluted with the 3.75 eV resolution of the

spectrometer. Table 6 contains the resonance parameters for the $(2p^2)^1D$ line measured in this work as well as the previous works. Figure 24 is a plot of the resonant excitation strength as a function of the atomic number of the ion. The values were calculated from the equations 5.17 and 5.22. From these experiments the enhancement factor for the BE electron peak was also determined for the hydrogen-like like boron, fluorine, magnesium and silicon. Low ion beam intensity prohibited the observation of the dominant $(2p^2)^1D$ line in hydrogen-like silicon. But the binary encounter electron peak for hydrogen-like and helium-like silicon was observed. These peaks were found to have an enhancement factor of 0.9 relative to the bare silicon ion in contrast to the measured value of 1.1 for the 1MeV/amu Si^{12+} and Si^{13+} projectiles [97]. Figure 25 shows the cross sections determined for the silicon ions and the fitted Rutherford cross sections. As is seen in the figure the measured cross sections do not entirely agree with the Rutherford calculation. This is believed to be due long integration time in collecting projectile ions since this may increase the number of background electrons collected. Rescattered electrons also appear to have contributed to the cross section as is apparent from the tails of the BE electrons peaks. The BE electron peak enhancement for various ions is presented in Table 7.

Figure 21 Measured doubly differential cross section for the collisions of the hydrogen-like magnesium ions with a thin molecular hydrogen target gas is depicted. The electron scattering model has been used to transform the electron-ion R-matrix calculation for this collision (the solid black line) [98] from the center of mass to the lab frame. The dash-dotted line is the classically calculated Rutherford cross section for an electron scattering from a central potential with an enhanced charge of $Z=1.05x11$. An increase in the measured cross section beyond 4000 eV is observed. This increase is most likely due to energetic electrons that are rescattered within the spectrometer since a background subtraction has not corrected this unexpected increase.

41.85 MeV Mg^{11+} + 30 mT H_2

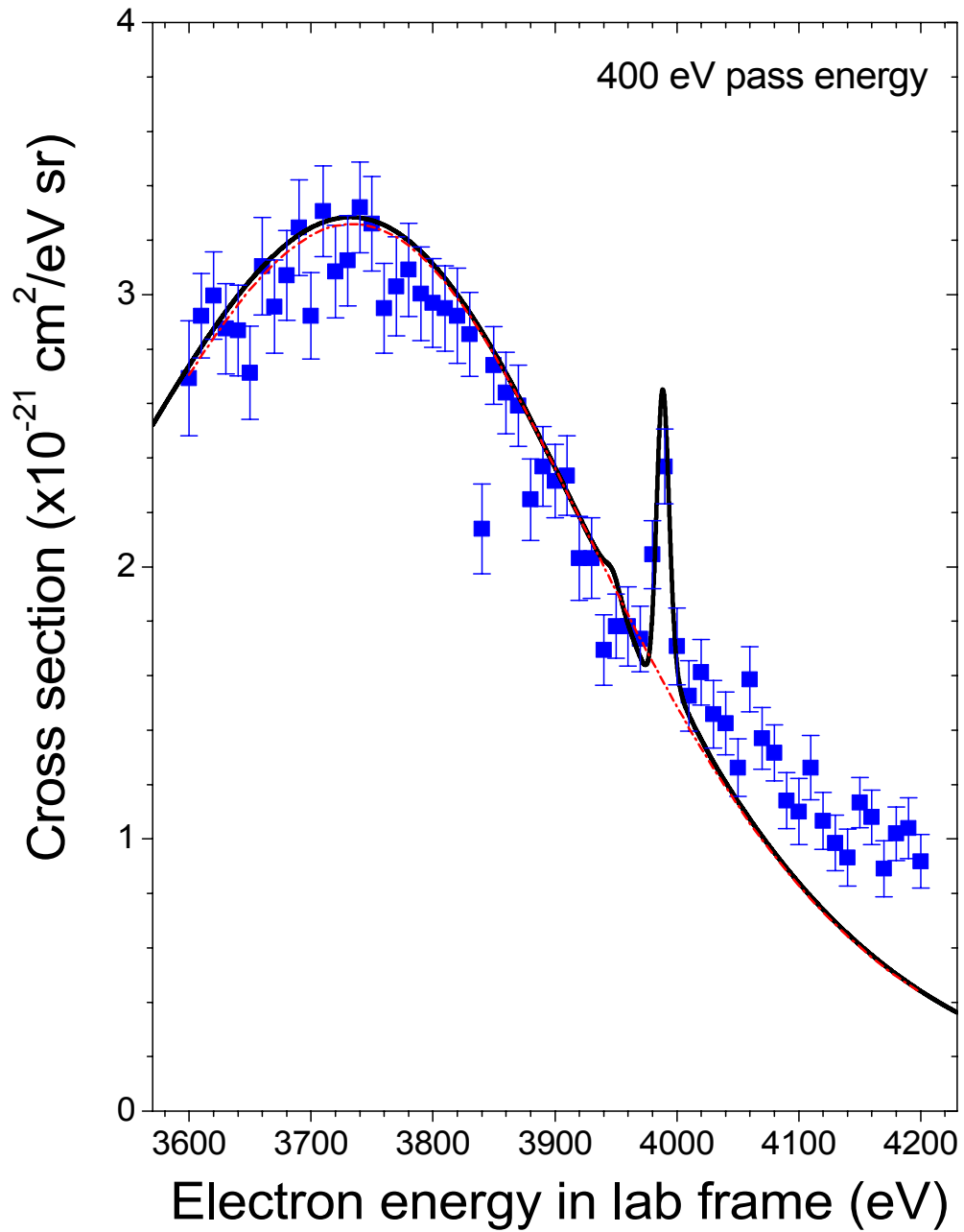


Figure 22 The differential cross sections of collisions of electrons with the hydrogen-like magnesium ions for the $2\ell 2\ell'$ manifold is depicted. These cross sections were calculated with the R-matrix method.

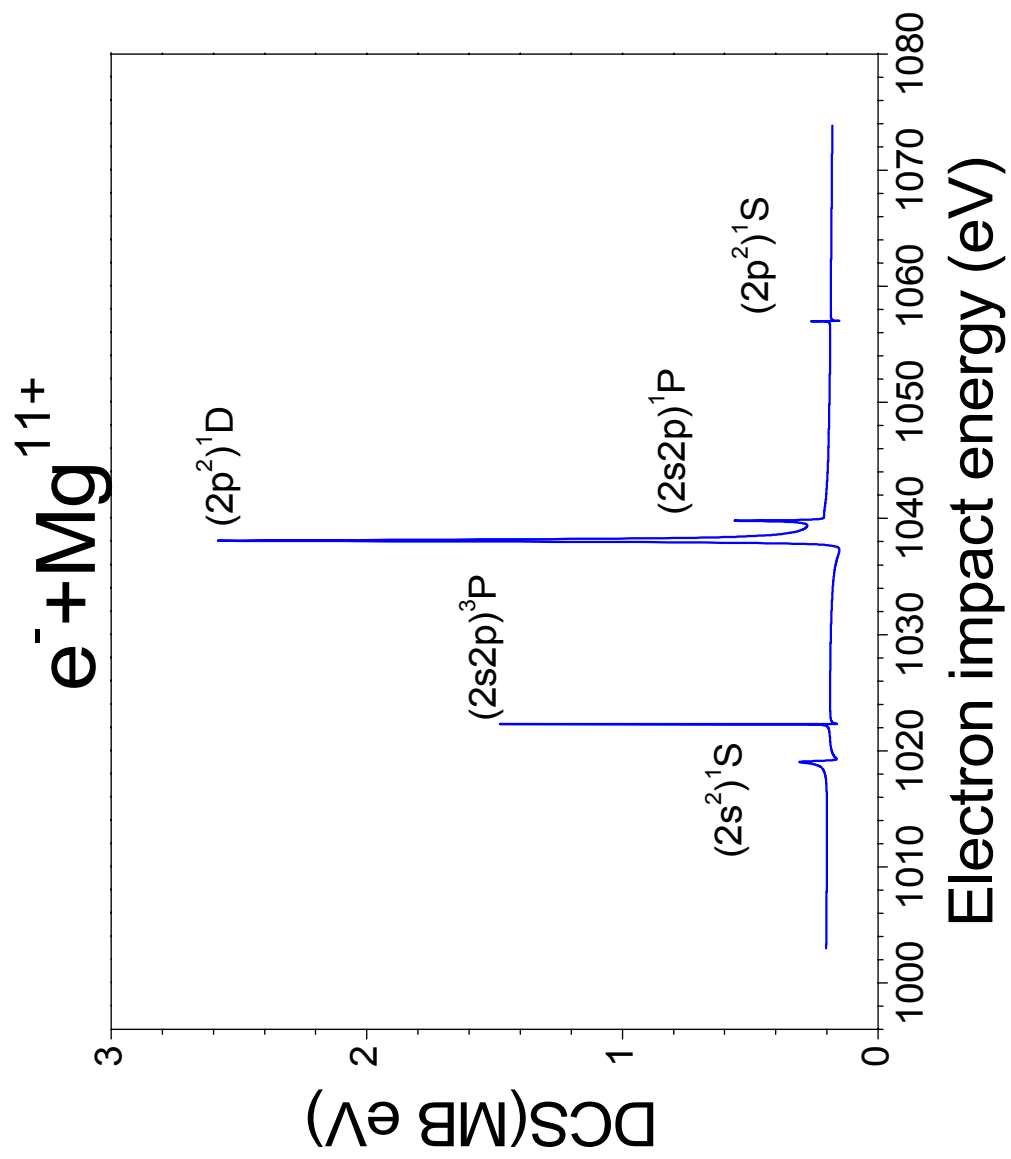
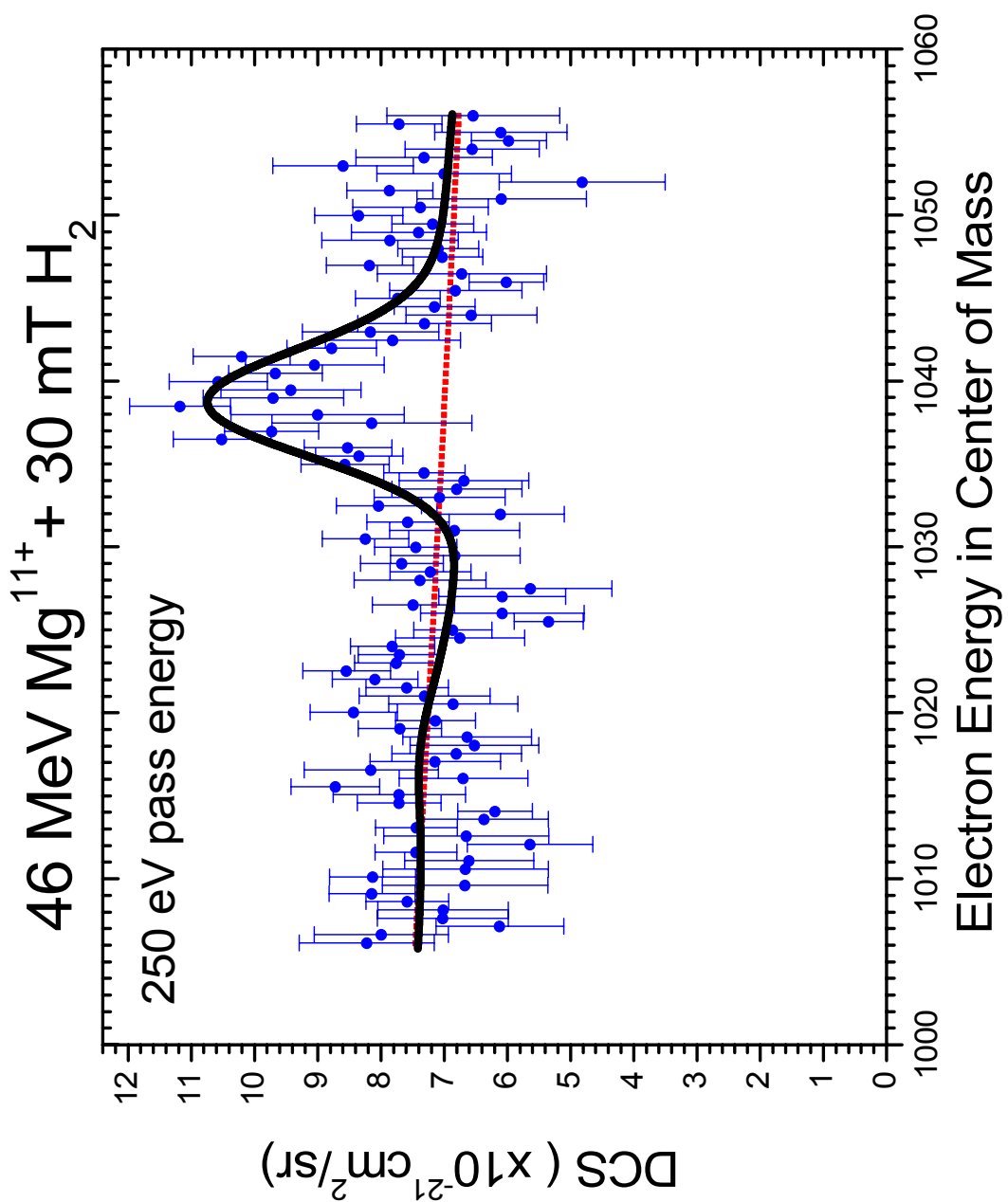


Figure 23 Experimental differential cross sections for the collisions of electrons with hydrogen-like magnesium ions is determined through collisions of hydrogen-like magnesium ions with a thin molecular hydrogen target gas. The same energy range depicted is the same as in the previous figure. The resolution of the experiment is such that only the $(2p^2)^1D$ term is visible.



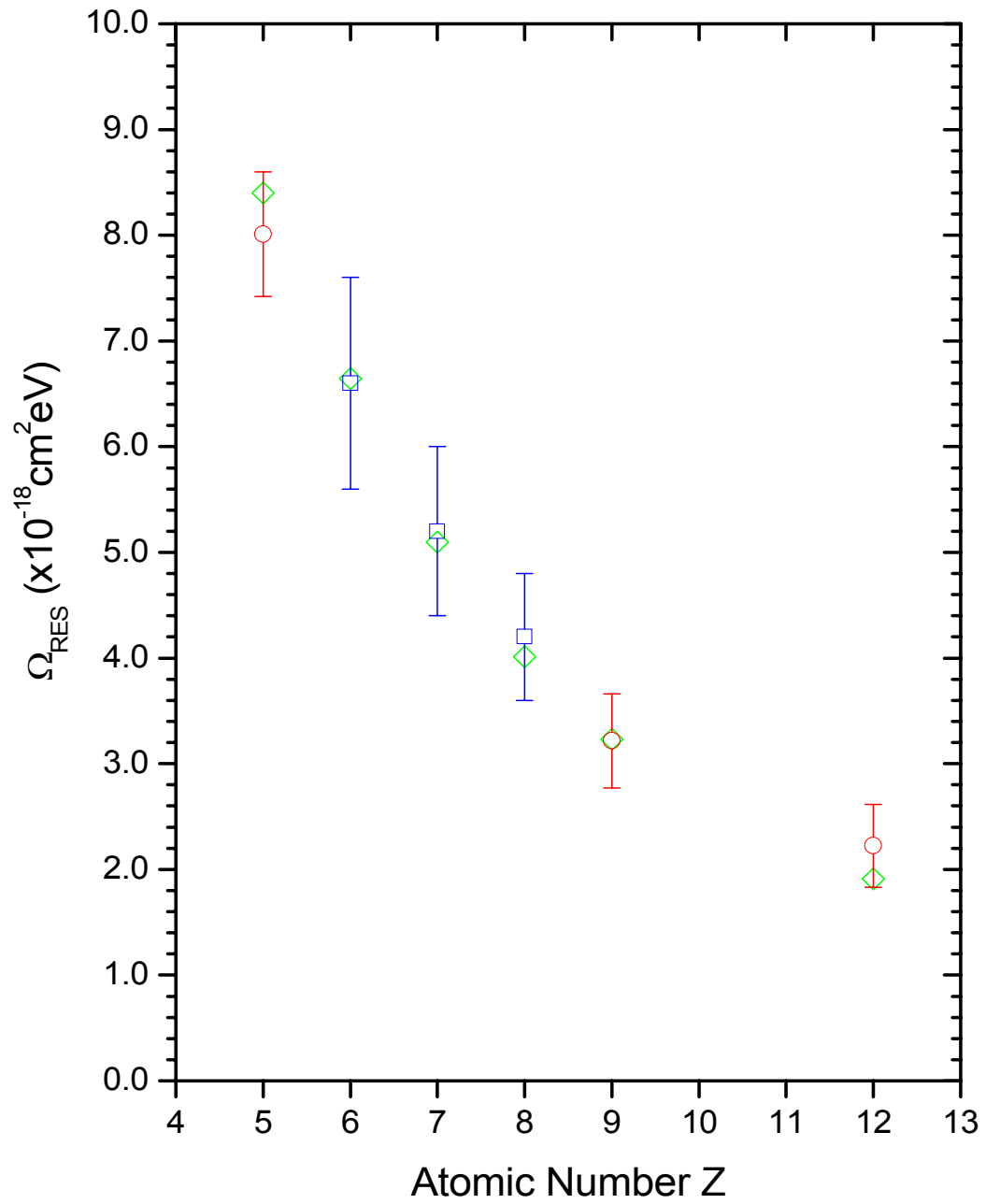
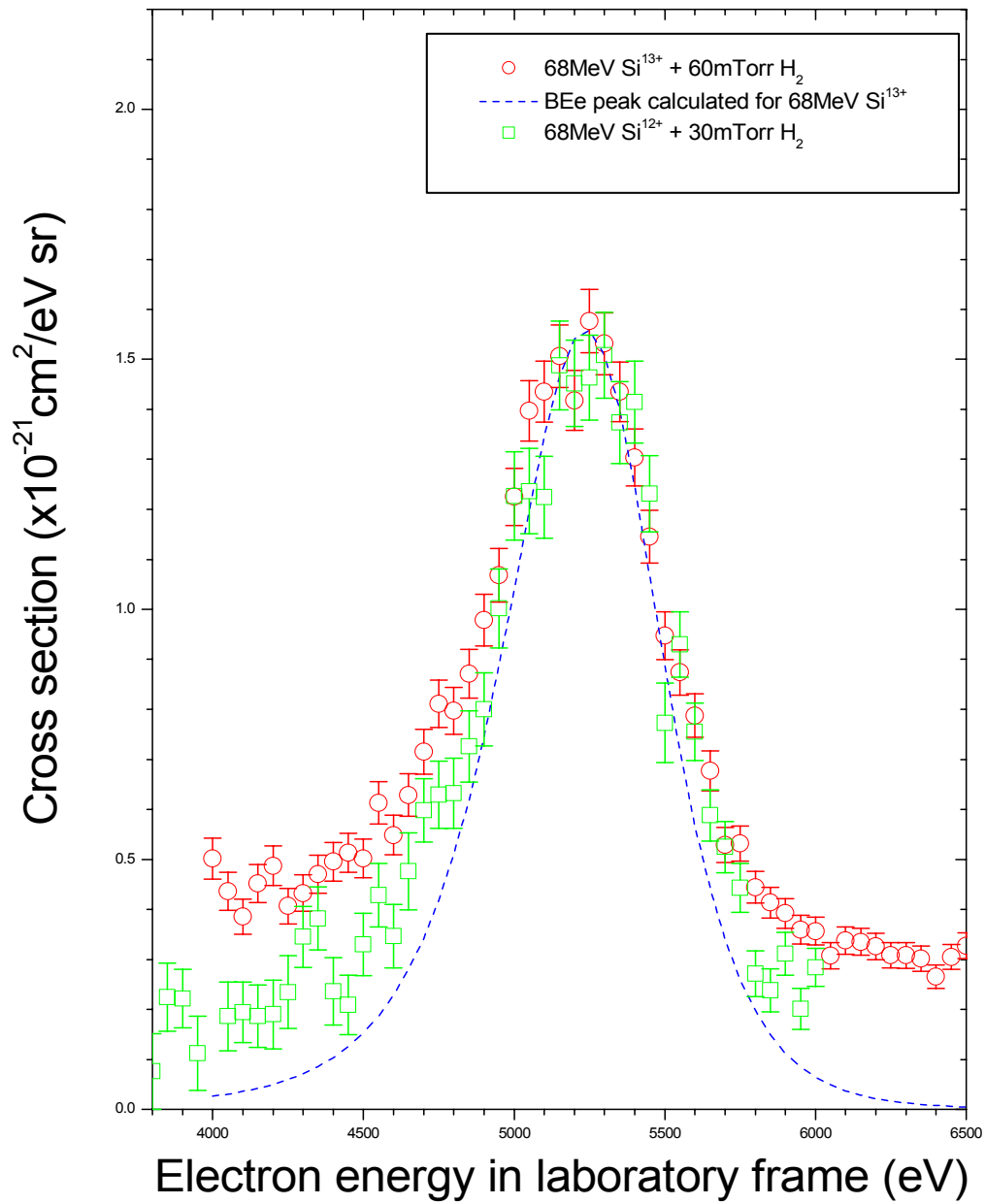


Figure 24 Resonant excitation strength for the $(2p^2)^1D$ line for various hydrogen-like ions. The ovals are the calculated theoretical values. The squares are the values obtained from previous experiments. The circles are measured values obtained in this work.

Figure 25 The measured cross sections of the BEe peaks for $\text{Si}^{12+,13+}$ presented in this picture. These cross sections are somewhat different from the predicted value due to the rescattered electrons entering the spectrometer. However both cross sections show the same enhancement in the projectile charge of about 0.95.



Ion	Z	E_A (eV)	A_r ($\times 10^{13}/s$)	A_a ($\times 10^{13}/s$)	ξ	Ω_{RES}^{Theory} ($\times 10^{-18} cm^2 \cdot eV$)	$\Omega_{RES}^{Experiment}$ ($\times 10^{-18} cm^2 \cdot eV$) Other work	$\Omega_{RES}^{Experiment}$ ($\times 10^{-18} cm^2 \cdot eV$) This work
B^{3+}	5	193.56 ^a	-	-	-	8.40	7.7 ± 1.6^c	8.01 ± 0.59
C^{4+}	6	273.3 ^b	0.148 ^b	29.5 ^b	0.995	6.65	6.6 ± 1.0^d	
N^{5+}	7	366.9 ^b	0.267 ^b	30.5 ^b	0.991	5.10	5.2 ± 0.8^d	
O^{6+}	8	474.2 ^b	0.456 ^b	31.2 ^b	0.986	4.01	4.2 ± 0.6^d	
F^{7+}	9	595 ^b	0.749 ^b	31.8 ^b	0.977	3.23	3.6 ± 0.5^d	3.22 ± 0.45
Mg^{11+}	12	1038.6 ^a	-	-		1.91		2.22 ± 0.39

Table 6 The $(2p^2)^1D$ line resonance parameters for various ions is presented. Z is the atomic number and E_A is the resonance Auger energy. A_r and A_a are the radiative and Auger decay rate and ξ is the Auger yield. a) from ref [98], b) from ref [97], c) from ref [99] and d) from ref [31].

Ion	R
$B^{4+}(1s)$	1.48
$F^{8+}(1s)$	1.16
$Mg^{11+}(1s)$	1.1
$Si^{13+}(1s)$	0.9
Si^{12+}	0.9

Table 7 The ratio of DDCS for non bare to bare ions, R, is known as the enhancement factor. This factor was determined for various ions from equation 4.1 having determined the detection efficiency of the spectrometer in advance (see Table 4). The relative error for the calculation of R is ~15%.

Resonant inelastic scattering

In the case of inelastic scattering the first two terms in equation 4 of reference 61 are eliminated. Thus the cross section for inelastic scattering is:

$$\begin{aligned} \frac{d\sigma_{if}}{d\Omega} = & \frac{1}{8(2L_i+1)(2S_i+1)k_i^2} \times \sum_{\lambda} (2\lambda+1) \left[\sum_{\ell_i, \ell_f, \ell'_i, \ell'_f} \begin{bmatrix} \ell_i & \ell'_i & \lambda \\ 0 & 0 & 0 \end{bmatrix} \begin{bmatrix} \ell_f & \ell'_f & \lambda \\ 0 & 0 & 0 \end{bmatrix} i^{(\ell_i-\ell_f)} i^{(\ell'_f-\ell'_i)} e^{i(\sigma_{\ell_i}-\sigma_{\ell'_i}+\sigma_{\ell'_f}-\sigma_{\ell_f})} \right. \\ & \left. \times \sum_{j_i} (-1)^{j_i+\lambda} (2j_i+1) \begin{Bmatrix} \ell_i & \ell_f & j_i \\ \ell'_f & \ell'_i & \lambda \end{Bmatrix} \sum_S M^* (\beta_i \ell'_i \beta_f \ell'_f j_i S) M (\beta_i \ell_i \beta_f \ell_f j_i S) \right] P_{\lambda}(\cos \theta) \end{aligned} \quad (5.23).$$

In this equation $M(\beta_i \ell_i \beta_f \ell_f j_i S)$ is defined by

$$\begin{aligned} M(\beta_i \ell_i \beta_f \ell_f j_i S) = & \sum_{\pi, L} (-1)^{\ell_i+\ell_f} [(2\ell_i+1)(2\ell_f+1)(2S+1)]^{1/2} \\ & \times (-1)^L (2L+1) \times \begin{Bmatrix} L_i & L_f & j_i \\ \ell_f & \ell_i & L \end{Bmatrix} T^{LS\pi}(\beta_i \rightarrow \beta_f) \end{aligned} \quad (5.24).$$

In these formulas k_i is the linear momentum of the incident electron. ℓ_i and ℓ_f are the orbital angular momenta of the incident and scattered electrons. β represents the quantum numbers in αLS , λ is the multipole anisotropy parameter in the differential cross section, ℓ is the free electron angular momentum and j_i is the momentum transfer quantum number [63]. S, L and π are the total spin, total angular momentum and parity of the (N+1) electron system and T is an element of the transition matrix \mathbf{T} .

Resonant inelastic scattering was studied in hydrogen-like boron prepared and accelerated through the Tandem Van de Graaff accelerator at energy sufficient to create a resonant electron capture and excitation of the boron ions to the $3\ell 3\ell'$ levels. Figure 26

shows the full zero degree electron spectrum of this experiment taken at low resolution. The electrons were decelerated in order to observe the $3\ell 3\ell'$ lines in high resolution. Figure 27 shows observed resonances in the center of mass of the ion. The theoretical calculation was done with the aid of an R-matrix approach to the close coupling calculation [60, 98]. Figure 28 shows theoretically calculated cross sections for $3\ell 3\ell'$ manifold with the individual terms identified. Figure 29 shows the theory convoluted with the 0.6 eV resolution of the spectrometer as well as the measured experimental data.

Figure 26 The full zero degree electron spectrum of collisions of hydrogen-like boron with a molecular hydrogen target can be seen here. The $2\ell 2\ell'$ and the $2\ell 3\ell$ manifolds can be seen on top of the BE electron peak. The $3\ell 3\ell'$ manifold is located on the high energy tail of the cusp peak. This manifold is only visible in the high resolution mode.

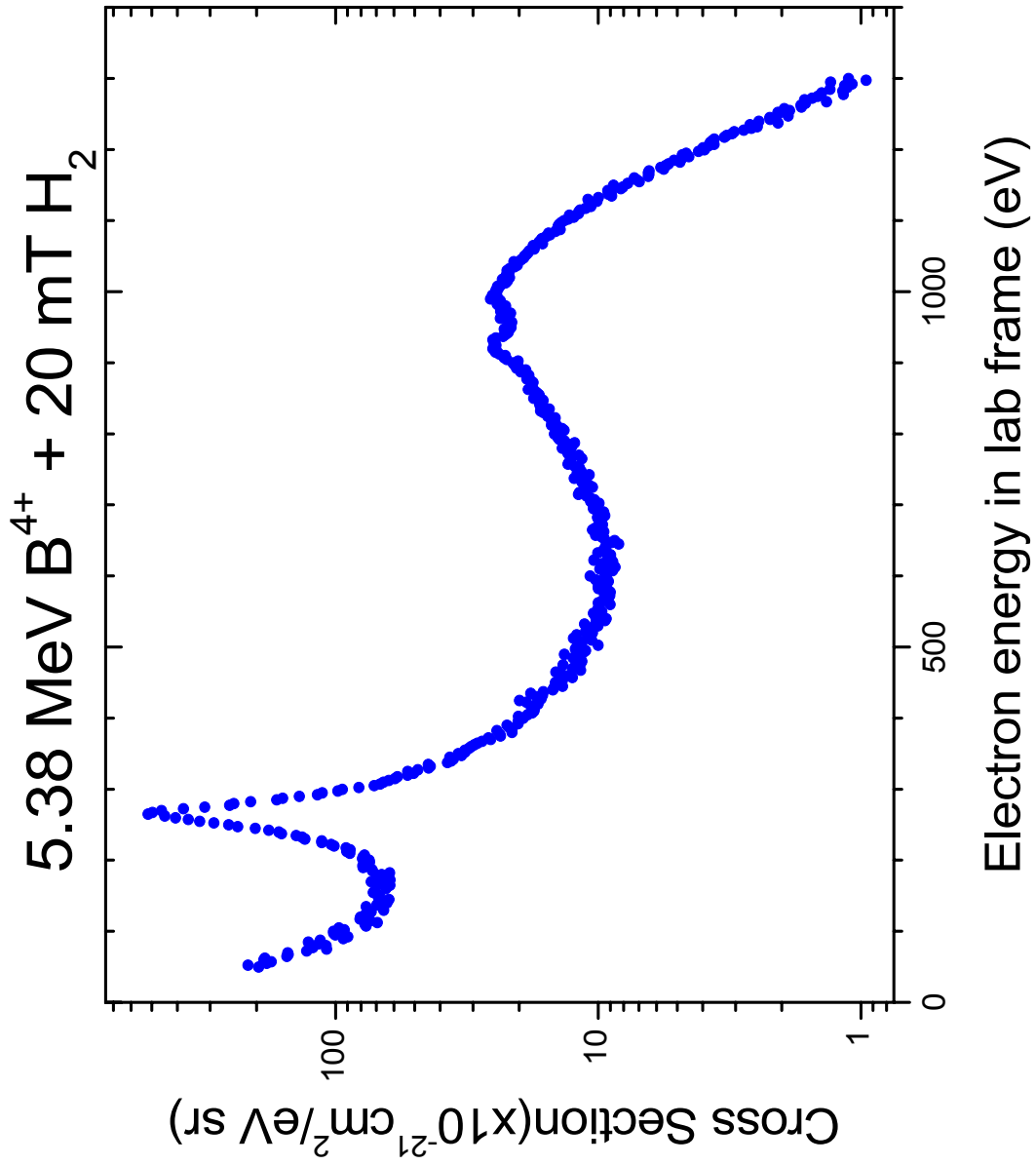


Figure 27 The differential cross sections for collisions of hydrogen-like boron with molecular hydrogen is depicted. Theoretical resonance electron impact excitation from the ground to the 2p level is seen to agree well with the $3\ell 3\ell'$ and $3\ell 4\ell$ resonances observed in the experiment.

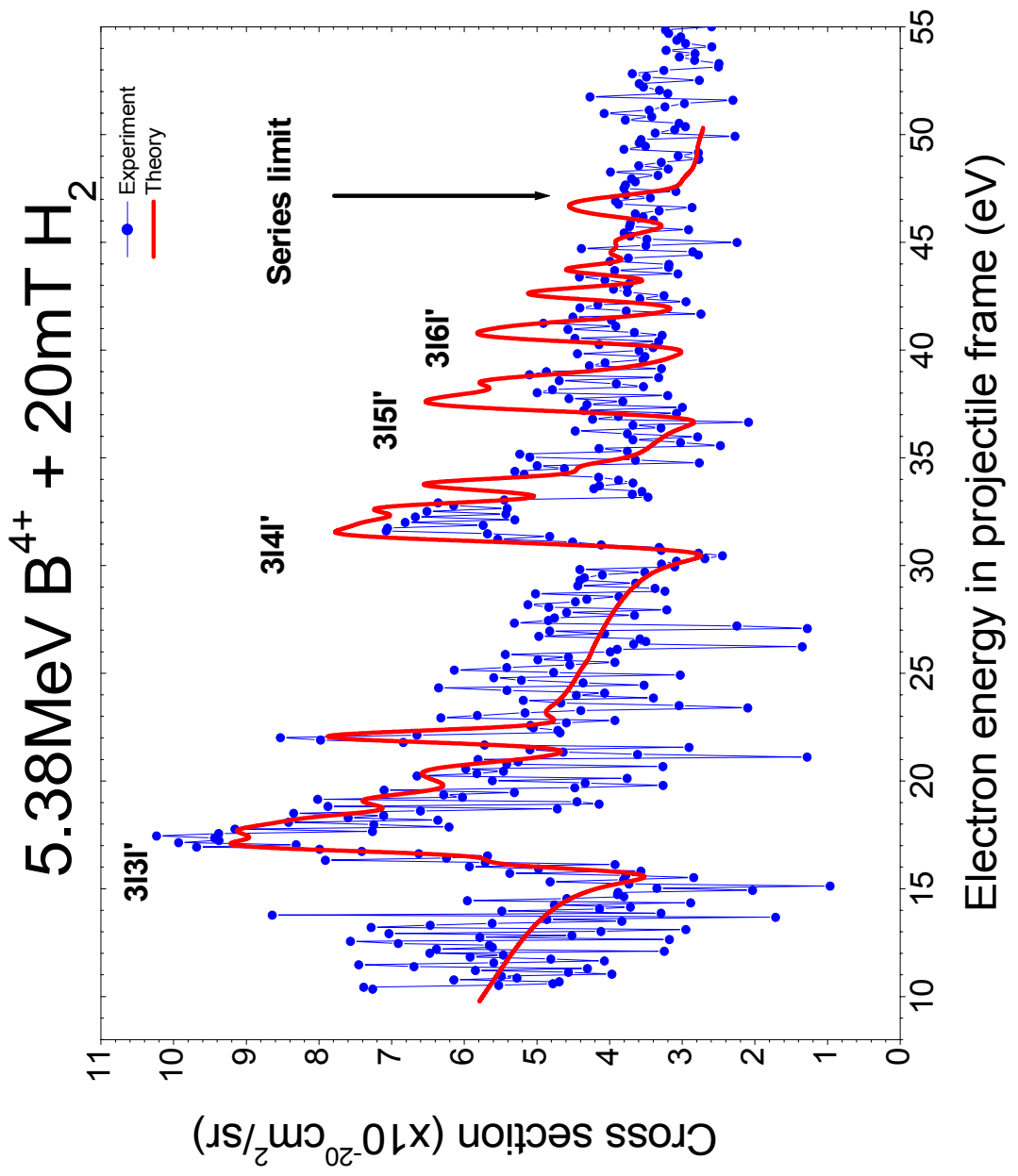


Figure 28 The theoretically calculated cross sections for the collisions of electrons with hydrogen-like boron ions differential in the solid angle is depicted. The $3\ell 3\ell'$ terms are identified in this picture.

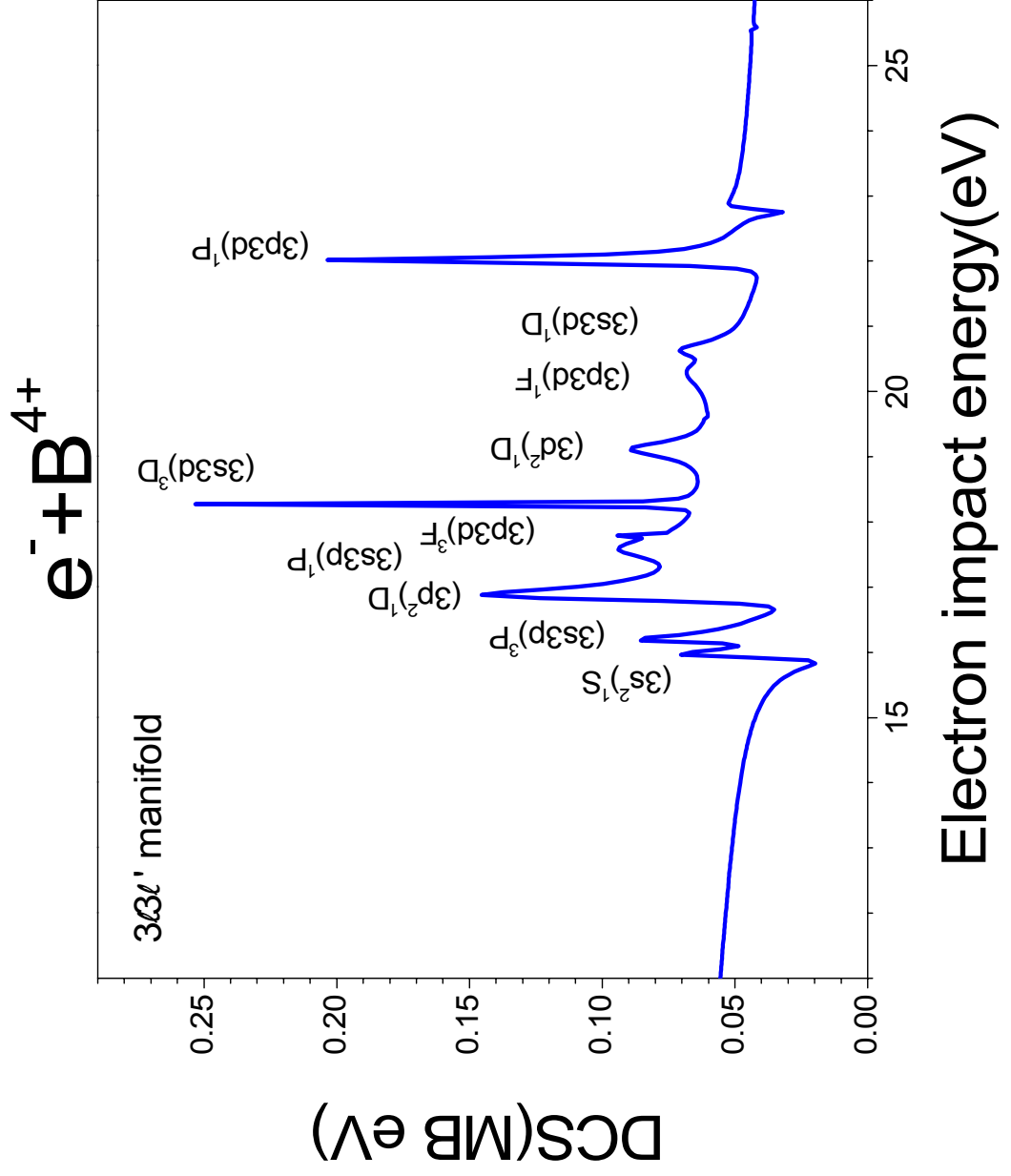
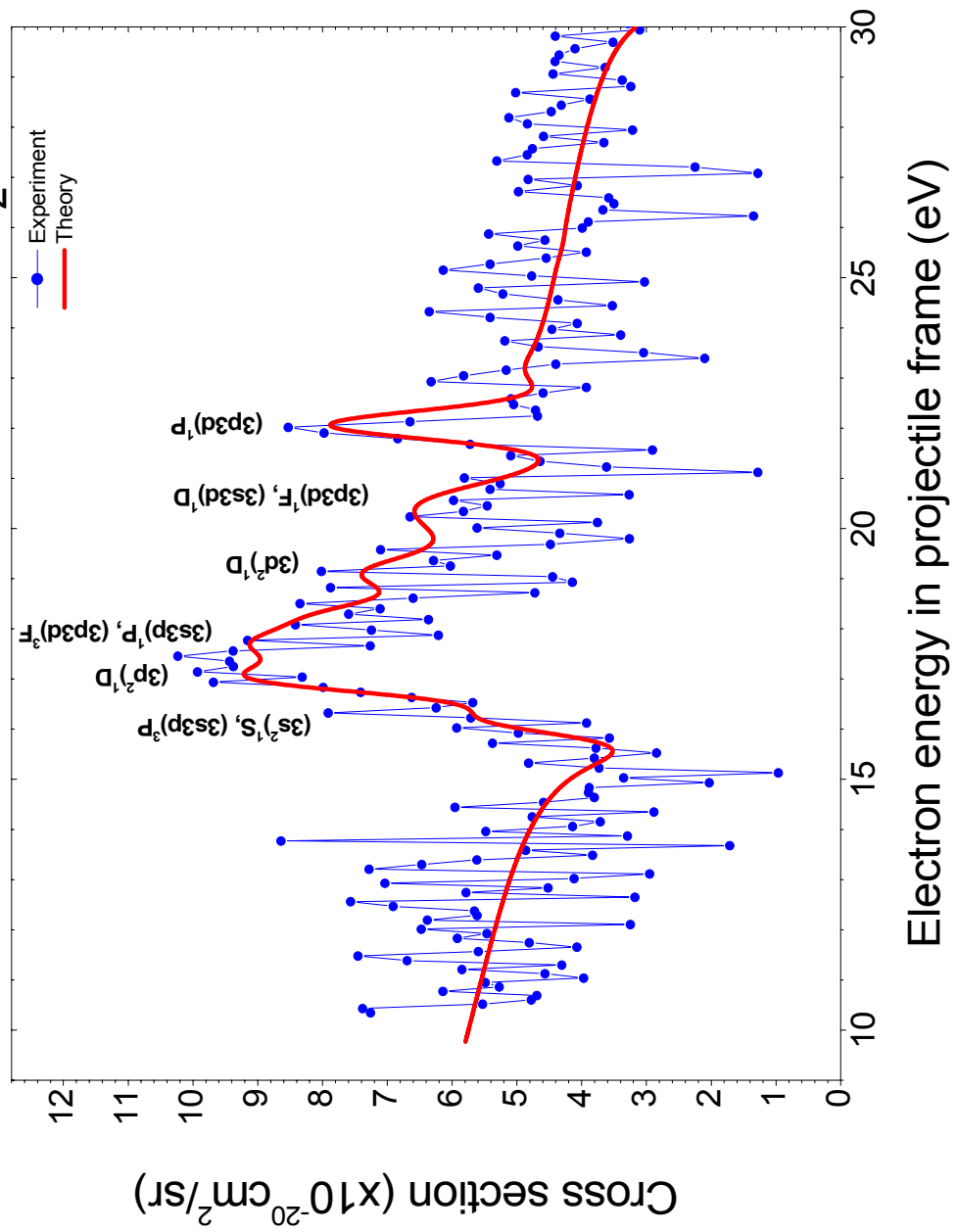


Figure 29 The measured cross sections as well as the theoretical calculation is shown in an expanded view. The terms of the $3\ell 3\ell'$ manifold are identified in this picture.

5.38MeV B⁴⁺ + 20mT H₂



Conclusions

The goals of this dissertation project were to 1) measure the elastic scattering of electrons from the highly charged ions of Mg^{11+} , Si^{12+} and Si^{13+} in order to extend our knowledge of resonant and non resonant electron scattering to this range from B^{q+} , C^{q+} , N^{q+} , O^{q+} and F^{q+} which have recently been published; 2) attempt to study inelastic electron scattering from these same ions even though these experiments seemed marginally possible; 3) extend the measurement of resonant inelastic electron scattering through $3\ell 3\ell'$ states down to the B^{4+} ion from the only previous studies of C^{5+} , O^{7+} and F^{8+} .

In order to accomplish these goals, particularly the first and the second goal, a new double parallel plate zero-degree high-resolution electron spectrometer with performance characteristics capable of handling the parameter space required by these experiments was designed and constructed. The major parameter was the high-voltage capabilities required to analyze the high-energy electrons required to reach these resonance states (i.e. electron energies greater than 3 keV in the laboratory frame). Another parameter was ease of spectrometer alignment. Alignment of the spectrometer plays a crucial role in reducing the number of background and rescattered electrons finding their way into the spectrometer. A final parameter improved was vacuum conditions. These goals were met by designing a system with better electrical properties, alignment capability and vacuum properties. The electrical insulation of the system was accomplished by using sufficiently large component spacing, using high quality ceramic

bolts and spacers and using polished conductor components. The alignment of the system was accomplished by staging the DPC and the spectrometer on tables capable of moving horizontally and vertically. These tables were used to align the system to better than 0.1 of an inch. The high vacuum requirement was accomplished by designing a new ultra efficient doubly differentially pumped chamber (the DPC) and a 12 cm long gas cell. The vacuum also accommodates small electron yield experiments by reducing the number of background electrons produced by the projectile-ion-background-gas scattering.

Following the construction and extensive testing of the new system, high-resolution zero-degree Auger-electron spectroscopy was conducted to measure resonance collision cross sections for hydrogen-like boron, magnesium and silicon ions. For the boron and magnesium studies, the direct 180° elastic electron scattering as well as the resonant 180° elastic electron scattering cross sections were measured and from these the resonant excitation strength for the $(2p^2)^1D$ resonance state was determined. The values of Ω_{RES} obtained are in agreement with the theoretical predictions assuming the direct and resonant scattering cross section may be treated separately with the interference of the two amplitudes contributing small amounts to the resonance cross section. Due to beam intensity limitations only direct scattering was observable in the case of silicon. By fitting the classical Rutherford scattering cross sections to the measured direct electron scattering cross sections for these ions enhancement factors for hydrogen-like ions as compared to the bare ions were obtained. In the case of boron a series resonant doubly-excited $3\ell n\ell'$ states corresponding to resonant inelastic scattering were observed. The calculated cross sections for electron impact excitation compares very well with the

$3\ell 3\ell'$ manifold. The observed discrepancy in the other measured manifolds may be due to the large background subtraction. This is due to the proximity of the resonance lines to the cusp electrons in the electron spectrum. The overall agreement of the theoretical results with the experimental measurements is further evidence that the current theoretical techniques adequately describe the electron-ion collision mechanisms in large angle scatterings.

References

1. K. T. Dolder and B. Perat, *Rep. Prog. Phys.* **39** (1976) 693.
2. R. S. Pease, *Contemp. Phys.* **18** (1977) 113.
3. A. Bocksenberg et al., *Nature* **275** (1978) 404.
4. D. E. Shemansky, *Astrophys. J.* **236** (1980) 1043.
5. G. H. Dunn, *The Physics of Ionized Gases*, edited by M. Matic, Boris Kidric Institute of Nuclear Sciences, Belgrade (1980).
6. *Applied Atomic Collision Physics*, vols. 1-5, Academic Press, London, 1982-1984.
7. D. E. Post, *Physics of Ion-Ion and Electron-Ion Collisions*, eds. F. Brouillard and J. McGowan, Plenum Press, New York (1983) 37.
8. D. L. Matthews et al, *Phys. Rev. Lett.* **54** (1985) 110.
9. B. H. Bransden and C. J. Joachain, *Physics of Atoms and Molecules*, Longman Scientific and Technical, Hong Kong (1991).
10. C. L. Cocke, *Review of Fundamental Processes and Application of Atoms and Ions*, ed. by C. D. Lin, World Scientific Publishing, Singapore (1993).
11. G. J. Pert, *Laser particle Beams* **12** (1994) 209.
12. F. P. Keenan, *Space Sci. Rev.* **75** (1996) 537.
13. A. Dsgupta, *Astrophys. J. (Suppl. Series)* **101** (1995) 401.
14. I. D. Williams, *Rep. Prog. Phys.* **62** (1999) 1431.
15. C. Belenger, P. Defrance, R. Friedlein, C. Guet, D. Jalabert, M. Maurel, C. Ristori, J. C. Rocco and B. A. Huber, *J. Phys. B* **29** (1996) 4433.
16. B. A. Huber, C. Ristori, C. Guet, D. Kichler, and W. R. Johnson, *Phys. Rev. Lett.* **73**, 2301 (1994).
17. J. B. Greenwood, I. D. Williams, and P. McGuinness, *Phys. Rev. Lett.* **75**, 1062 (1995).
18. M. Kuzel, R. D. DuBois, R. Maier, O Heil, D. H. Jakubassa-Amundsen, M. W. Lucas and K. O. Groeneveld, *J. Phys. B* **27** (1994) 1993.
19. P. A. Zavodszky, P. Richard, C. P. Bhalla, *Nucl. Instrum. Meth. Phys. Res. B* **154** (1999) 153.
20. P. A. Zavodszky, H. Aliabadi, C. P. Bhalla, P. Richard, *Phys. Rev. Lett.* **87** (2001) 033202-1.
21. D. Brandt, *Phys. Rev. A.* **27** (1983) 1314.
22. P. Auger, *Compt. Rend.* **177** (1923) 169.
23. E. H. S. Burhop, *The Auger effect and Other Radiationless Transitions*, Cambridge University Press, 1952.
24. H. S. W. Massey and D. R. Bates, *Rep. Prog. Phys.* **9** (1943) 62.
25. M. J. Seaton and P. J. Stoney, *Dielectronic Recombination in Atomic Processes and Applications*, ed. P. G. Burke and B. L. Moisewitsch (North Holland, Amsterdam, 1976) 135.
26. R. Ali, C. P. Bhalla, C. L. Cocke, and M. Stockli, *Phys. Rev. Lett.* **64** (1990) 633.
27. G. N. Ogursov, *Rev. Mod. Phys.* **44** (1972) 1.

28. N. Stolterfoht, *Phys. Rep.* 146 (1987) 315.
29. N. Stolterfoht, R. D. DuBois and R. D. Rivarola, *Electron Emission in Heavy Ion-Atom Collisions*, Springer, Berlin, 1997.
30. H. Aliabadi, R. Unal, M. Zamkov, P. Richard, C. P. Bhalla, H. Tawara, M. Gealy and A. T. Hassan, *AIP Conf. Proc.* 576 (2001) 172.
31. G. Toth, P. Zavodszky, C. P. Bhalla, P. Richard, S. Grabbe and H. Aliabadi, *Phys. Scr. T* 92 (2001) 272.
32. D. H. Lee, T. J. M. Zouros, J. M. Sanders, J. L. Shinpaugh, T. N. Tipping, S. L. Varghese, B. D. Depaola and P. Richard, *Nucl. Instrum. Meth. Phys. Res. Sec. B.* 40/41 (1989) 1229.
33. D. H. Lee, P. Richard, T. J. M. Zouros, J. M. Sanders, J. L. Shinpaugh, and H. Hidmi, *Phys. Rev. A* 41 (1990) 4816.
34. M. Inokuti, *Rev. Mod. Phys.* 43 (1971) 297.
35. N. F. Mott and H. S. W. Massey, *The Theory of Atomic Collisions*, Oxford University Press, Oxford, 1965.
36. J. A. Tanis, S. M. Shafroth, J. E. Willis, M. Clark, J. Swenson, E. Strait and J. R. Mowat, *Phys. Rev. Lett.* 47 (1981) 828.
37. J. A. Tanis, E. M. Bernstein, W. G. Graham, M. Clark, S. M. Shafroth, B. M. Johnson, K. W. Jones and M. Meron, *Phys. Rev. Lett.* 49 (1982) 1325.
38. J. K. Swenson, Y. Yamazaki, P. D. Miller, H. F. Krause, P. F. Dittner, P. L. Pepmiller, S. Datz and N. Stolterfoht, *Phys. Rev. Lett.* 57 (1986) 3042.
39. M. Clark, D. Brandt, J. K. Swenson and S. M. Shafroth, *Phys. Rev. Lett.* 54 (1985) 544.
40. P. L. Pepmiller, P. Richard, J. Newcomb, T. R. Dillingham, J. M. Hall, T. J. Gray and M. Stockli, *IEEE Trans. Nucl. Sci. NS-30* (1983) 1002.
41. T. J. M. Zouros, D. H. Lee, P. Richard, J. M. Sanders, J. L. Shinpaugh, S. L. Varghese, K. R. Karim and C. P. Bhalla, *Phys. Rev. A* 40 (1989) 6246.
42. J.M. Feagin, J. S. Briggs and T. M. Reeves, *J. Phys. B* 17 (1984) 1057.
43. C. P. Bhalla, *Phys. Rev. Lett.* 64 (1990) 1103.
44. P. Richard, C. P. Bhalla, S. Hagmann and P. A. Zavodszky, *Phys. Scr. T* 80 (1999) 87.
45. P. Hvelplund, A. D. Gonzales, P. Dahl, C. P. Bhalla, *Phys. Rev. A* 49 (1994) 2535.
46. G. Kilgus, J. Berger, P. Blatt, M. Grieser, D. Habs, B. Hochadel, E. Jaeschke, D. Kramer, R. Neumann, G. Neureither, W. Ott, D. Schwalm, M. Steck, R. Stokstad, A. Wolf, R. Schuch, A. Muller and M. Wagner, *Phys. Rev. Lett.* 64 (1990) 737.
47. G. Kilgus, D. Habs, D. Schwalm, A. Wolf, N. R. Bandell, A. Muller, *Phys. Rev. A* 46 (1992) 5730.
48. D. H. Lee, Ph.D. Dissertation, Department of Physics, Kansas State University, 1990, Unpublished.
49. D. E. Golden and H. W. Bandel, *Physical Review* 138 (1965) A14.
50. K.D. Sevier, *Low Energy Electron Spectrometry* (Wiley, New York, 1972).
51. A. Itoh, D. Schneider, T. Schneider, T.J.M. Zouros, G. Nolte, G. Schiweitz, Z. Zeitz and N. Stolterfoht, *Phys. Rev. A* 31, 684 (1985).

52. Conversations with Dr. Peter Zavodszky, Professor Richard, and other colleagues.
53. See for example Alfa Aesar Research Chemicals, Metals and Materials catalogue 1997-98, p. 1268. Typically for high purity oxide ceramics the electrical breakdown strength is rated at 22 kV/mm or higher.
54. K.R. Symon, *Mechanics* (Addison-Wesley, Reading, 1971).
55. Information provided by Professor K. D. Carnes of the J. R. Macdonald Laboratory.
56. B. Sulik, Cs. Koncz, K. Tokesi, A. Orban, D. Berenyi, *Phys. Rev. Lett.* **88** (2002) 073201.
57. B. Sulik, Cs. Koncz, K. Tokesi, A. Orban, A. Kover, S. Ricz, N. Stolterfoht, R. Hellhammer, J.-Y. Chesnel, P. Richard, H. Tawara, H. Aliabadi, D. Berenyi, *AIP Conf. Proc.* **652** (2003) 195.
58. P. Richard, D. H. Lee, T. J. M. Zouros, J. M. Sanders, and J. L. Shinpaugh, *J. Phys. B* **23** (1990) L213.
59. C. P. Bhalla, *Phys. Rev. Lett.* **64** (1990) 1103.
60. E. P. Benis et al., *Phys. Rev. A*, to be published.
61. D. C. Griffin, M. S. Pindzola, *Phys. Rev. A* **42** (1990) 248.
62. D. C. Griffin, M. S. Pindzola and N. R. Badnell, *Phys. Rev. A* **47** (1993) 2781.
63. S. A. Salvini, *Comput. Phys. Commun.* **64** (1991) 364.
64. C. P. Bhalla, R. Shingal, *J. Phys. B* **24** (1991) 3187.
65. P. D. Fainstein, V. H. Ponce, *Phys. Rev. A* **45** (1992) 6417.
66. H. I. Hidmi, C. P. Bhalla, S. R. Grabbe, J. M. Sanders, P. Richard, R. Shingal, *Phys. Rev. A* **47** (1993) 2398.
67. J. Macek, Knud Taulbjerg, *J. Phys. B* (1993) 1353.
68. C. Liao, P. Richard, S. R. Grabbe, C. P. Bhalla, T. J. M. Zouros and S. Hagmann, *Phys. Rev. A* **50** (1994) 1328.
69. L. Gulyas, P. D. Fainstein, *J. Phys. B* **31** (1998) 3297.
70. A. Chutjian and W. R. Newell, *Phys. Rev. A* **26** (1982) 2271.
71. A. Z. Msezane and R. J. W. Henry, *Phys. Rev. A* **25** (1982) 692.
72. A. Chutjian, A. Msezane, R. J. W. Henry, *Phys. Rev. Lett.* **50** (1983) 1357.
73. A. Chutjian, *Phys. Rev. A* **29** (1984) 64.
74. I. D. Williams, A. Chutjian, R. J. Mawhorter, *J. Phys. B* **19** (1986) 2189.
75. B. A. Huber, Ch. Ristori, P. A. Hervieux, M. Maurel, C. Guet, H. Andra, *Phys. Rev. Lett.* **67** (1991) 1407.
76. X. Q. Guo, E. W. Bell, J. S. Thompson, G. H. Dunn, M. E. Bannister, R. A. Phaneuf, A. C. H. Smith, *Phys. Rev. A* **47** (1993) R9.
77. Y. Hahn, K. J. La Gattuta, *Phys. Rep.* **166** (1988) 195.
78. D. A. Knapp, R. E. Marrs, M. A. Levine, C. L. Bennett, M. H. Chen, J. R. Henderson, M. B. Schneider, J. H. Scofield, *Phys. Rev. Lett.* **62** (1989) 2104.
79. T. Mohamed, D. Nikolic, E. Lindroth, S. Madzunkov, M. Fogle, M. Tokman, R. Schuch, *Phys. Rev. A* **66** (2002) 022719.
80. C. Brandau, T. Bartsch, A. Hoffknecht, H. Knopp, S. Schippers, W. Shi, A. Muller, N. Grun, W. Scheid, T. Steih, F. Bosch, B. Franzake, C. Kozhuharov, P. H. Mokler, F. Nolden, M. Steck, T. Stohlker, Z. Stachura, *Phys. Rev. Lett.* **89** (2002) 053201.

81. M. Tokman, N. Eklow, P. Glans, E. Lindroth, R. Schuch, G. Gwinner, D. Schwalm, A. Wolf, A. Hoffknecht, A. Muller, S. Schippers, *Phys. Rev. A* **66** (2002) 012703.
82. J. S. Lee, *J. Chem. Phys.* **66** (1977) 4906.
83. F. Drepper, J. S. Briggs, *J. Phys. B* **9** (1976) 2063.
84. N. Stolterfoht, *Phys. Rep.* **146** (1987) 315.
85. T. J. M. Zouros, *Recombination of Atomic ions*, Vol. 296 of NATO Advanced Study Institute Series B: Physics, edited by W. G. Graham, W. Fritsch, Y. Hahn, J. A. Tanis (Plenum, New York, 1992).
86. Y. Hahn, *Phys. Rev. A* **40** (1989) 2950.
87. A. M. Burgess, *Astrophys. J.* **141** (1965) 1588.
88. B. W. Shore, *Astrophys. J.* **158** (1969) 1205.
89. Y. Hahn, *Adv. At. Mol. Phys.* **21** (1985) 123.
90. Y. Hahn, *Comments At. & Mol. Phys.* **19**, No. 2, (1987) 99.
91. B. Cleff and W. Melhorn, *J. Phys. B* **7** (1974) 593.
92. W. Melhorn, *University of Aarhus Lecture Notes*, University of Aarhus, Aarhus, Denmark (1978).
93. T. J. M. Zouros, C. P. Bhalla, D. H. Lee, P. Richard, *Phys. Rev. A* **42** (1990) 678.
94. C. P. Bhalla, S. R. Grabbe, A. K. Bhatia, *Phys. Rev. A* **52** (1995) 2109.
95. P. A. Zavodszky, G. Toth, S. R. Grabbe, T. J. M. Zouros, P. Richard, C. P. Bhalla, J. A. Tanis, *J. Phys. B* **32** (1999) 4425.
96. C. P. Bhalla and T. W. Tunnel, *J. Quant. Spectrosc. Radiat. Transfer* **32** (1984) 141.
97. H. I. Hidmi, Ph.D. Dissertation, Kansas State University (1993), Unpublished.
98. R-matrix calculations performed by Professor T. W. Gorczyca.
99. E. P. Benis, Ph.D. Dissertation, University of Crete (2001), Unpublished.